Monthly Notices
of the
ROYAL ASTRONOMICAL SOCIETY

Mon. Not. R. Astron. Soc. **417,** 1787–1816 (2011) doi:10.1111/j.1365-2966.2011.19372.x

The SAURON project – XIX. Optical and near-infrared scaling relations of nearby elliptical, lenticular and Sa galaxies

J. Falcón-Barroso,[1,2,3]★ G. van de Ven,[4,5] R. F. Peletier,[6] M. Bureau,[7] H. Jeong,[8,9] R. Bacon,[10] M. Cappellari,[7] R. L. Davies,[7] P. T. de Zeeuw,[11,12] E. Emsellem,[10,11] D. Krajnović,[11] H. Kuntschner,[13] R. M. McDermid,[14] M. Sarzi,[15] K. L. Shapiro,[16,17] R. C. E. van den Bosch,[4] G. van der Wolk,[6] A. Weijmans[18]† and S. Yi[19]

[1] *Instituto de Astrofísica de Canarias, Vía Láctea s/n, La Laguna, Tenerife, Spain*
[2] *Departamento de Astrofísica, Universidad de La Laguna, E-38205 La Laguna, Tenerife, Spain*
[3] *European Space and Technology Centre, Keplerlaan 1, 2200 AG Noordwijk, the Netherlands*
[4] *Max Planck Institute for Astronomy, Königstuhl 17, 69117 Heidelberg, Germany*
[5] *Institute for Advanced Study, Einstein Drive, Princeton, NJ 08540, USA*
[6] *Kapteyn Astronomical Institute, University of Groningen, Postbus 800, 9700 AV Groningen, the Netherlands*
[7] *Sub-Department of Astrophysics, Department of Physics, University of Oxford, Denys Wilkinson Building, Keble Road, Oxford OX1 3RH*
[8] *Korea Astronomy and Space Science Institute, Daejeon 305-348, Korea*
[9] *Yonsei University Observatory, Seoul 120-749, Korea*
[10] *Université Lyon 1, Observatoire de Lyon, Centre de Recherche Astrophysique de Lyon and Ecole Normale Supérieure de Lyon, 9 avenue Charles André, F-69230 Saint-Genis Laval, France*
[11] *European Southern Observatory, Karl-Schwarzschild-Str. 2, 85748 Garching, Germany*
[12] *Sterrewacht Leiden, Leiden University, Postbus 9513, 2300 RA Leiden, the Netherlands*
[13] *Space Telescope European Coordinating Facility, European Southern Observatory, Karl-Schwarzschild-Str. 2, 85748 Garching, Germany*
[14] *Gemini Observatory, Northern Operations Centre, 670 North A'ohoku Place, Hilo, HI 96720, USA*
[15] *Centre for Astrophysics Research, University of Hertfordshire, Hatfield, Herts AL1 9AB*
[16] *Department of Astronomy, University of California-Berkeley, Berkeley, CA 94720, USA*
[17] *Aerospace Research Laboratories, Northrop Grumman Aerospace Systems, Redondo Beach, CA 90278, USA*
[18] *Dunlap Institute for Astronomy & Astrophysics, University of Toronto, 50 St. George Street, Toronto, ON M5S 3H4, Canada*
[19] *Department of Astronomy, Yonsei University, Seoul 120-749, Korea*

Accepted 2011 July 1. Received 2011 June 21; in original form 2011 January 27

ABSTRACT

We present ground-based MDM Observatory V-band and *Spitzer*/InfraRed Array Camera 3.6-μm-band photometric observations of the 72 representative galaxies of the SAURON survey. Galaxies in our sample probe the elliptical E, lenticular S0 and spiral Sa populations in the nearby Universe, both in field and cluster environments. We perform aperture photometry to derive homogeneous structural quantities. In combination with the SAURON stellar velocity dispersion measured within an effective radius (σ_e), this allows us to explore the location of our galaxies in the colour–magnitude, colour–σ_e, Kormendy, Faber–Jackson and Fundamental Plane scaling relations. We investigate the dependence of these relations on our recent kinematical classification of early-type galaxies (i.e. slow/fast rotators) and the stellar populations. Slow rotator and fast rotator E/S0 galaxies do not populate distinct locations in the scaling relations, although slow rotators display a smaller intrinsic scatter. We find that Sa galaxies deviate from the colour–magnitude and colour–σ_e relations due to the presence of dust, while the E/S0 galaxies define tight relations. Surprisingly, extremely young objects do not display the bluest ($V - [3.6]$) colours in our sample, as is usually the case in optical colours. This can be understood in the context of the large contribution of thermally pulsing asymptotic giant branch stars to the infrared, even for young populations, resulting in a very tight

---

★E-mail: jfalcon@iac.es
†Dunlap Fellow.

$(V-[3.6])$–$\sigma_{\rm e}$ relation that in turn allows us to define a strong correlation between metallicity and $\sigma_{\rm e}$. Many Sa galaxies appear to follow the Fundamental Plane defined by E/S0 galaxies. Galaxies that appear offset from the relations correspond mostly to objects with extremely young populations, with signs of ongoing, extended star formation. We correct for this effect in the Fundamental Plane, by replacing luminosity with stellar mass using an estimate of the stellar mass-to-light ratio, so that all galaxies are part of a tight, single relation. The new estimated coefficients are consistent in both photometric bands and suggest that differences in stellar populations account for about half of the observed tilt with respect to the virial prediction. After these corrections, the slow rotator family shows almost no intrinsic scatter around the best-fitting Fundamental Plane. The use of a velocity dispersion within a small aperture (e.g. $R_{\rm e}/8$) in the Fundamental Plane results in an increase of around 15 per cent in the intrinsic scatter and an average 10 per cent decrease in the tilt away from the virial relation.

Key words: galaxies: bulges – galaxies: elliptical and lenticular, cD – galaxies: fundamental parameters – galaxies: photometry – galaxies: stellar content – galaxies: structure.

1 INTRODUCTION

Galaxies are fundamental building blocks of our Universe, and our knowledge of their distribution, structure and dynamics is closely tied to our general understanding of structure growth. The so-called scaling relations, that is, correlations between well-defined and easily measurable galaxy properties, have always been central to our understanding of nearby galaxies. With high-redshift studies now routine, scaling relations are more useful than ever, allowing us to probe the evolution of galaxy populations over a large range of look-back times (e.g. Bell et al. 2004; Conselice et al. 2005; Ziegler et al. 2005; Saglia et al. 2010).

The colour–magnitude relation (CMR) was already recognized in the 1960s and 1970s (de Vaucouleurs 1961; Sandage 1972; Visvanathan & Sandage 1977) and has since then served as an important benchmark for theories of galaxy formation and evolution (e.g. Bower, Lucey & Ellis 1992; Bell et al. 2004; Bernardi et al. 2005). The main drivers are thought to be galaxy metallicity, which causes more-metal-rich galaxies to be redder, and age, causing younger galaxies to be bluer. Galaxies devoid of star formation are thought to populate the red sequence, while star-forming galaxies lie in the blue cloud (e.g. Baldry et al. 2004). The dichotomy in the distribution of galaxies in this relation has opened a very productive avenue of research to unravel the epoch of galaxy assembly (e.g. De Lucia et al. 2004; Andreon 2006; Arnouts et al. 2007).

Since its discovery (Djorgovski & Davis 1987; Dressler et al. 1987), the Fundamental Plane (FP) has been one of the most studied relations in the literature. Given its tightness, like many other scaling relations, the FP was quickly envisaged as a distance estimator as well as a correlation to understand how galaxies form and evolve (e.g. Saglia, Bender & Dressler 1993; Jørgensen, Franx & Kjaergaard 1996; Pahre, Djorgovski & de Carvalho 1998; Kelson et al. 2000; Bernardi et al. 2003b; van der Wel et al. 2004; Holden et al. 2005; MacArthur et al. 2010). It is widely recognized that the FP is a manifestation of the virial theorem for self-gravitating systems averaged over space and time with the physical quantities total mass, velocity dispersion and gravitational radius replaced by the observables mean effective surface brightness ($\langle\mu_{\rm e}\rangle$), effective (half-light) radius ($R_{\rm e}$) and stellar velocity dispersion (σ). Since velocity dispersion and surface brightness are distance-independent quantities, contrary to effective radius, it is common to express the FP as $\log(R_{\rm e}) = \alpha\log(\sigma) + \beta\langle\mu_{\rm e}\rangle + \gamma$, to separate distance errors from others. If galaxies were homologous with constant total mass-to-light ratios, then the FP would be equivalent to the virial plane and be infinitely thin, with slopes $\alpha = 2$ and $\beta = 0.4$ (in the notation used here). By studying the intrinsic scatter around the FP, one can study how galaxy properties differ within the observed sample.

Some projections of the FP, known earlier in time, have also been widely studied. Kormendy (1977) found that the surface brightness density (i.e. mean surface brightness) of a galaxy changes as a function of its size. This relation is usually known as the Kormendy relation (KR). The correlation is such that larger galaxies have lower surface brightness densities, compared to their smaller counterparts. The size–luminosity relation (SLR) is widely used to establish the size evolution of galaxies as a function of redshift (e.g. Trujillo et al. 2006; van Dokkum et al. 2008). Finally, the last projection of the FP that we consider in this paper is the Faber–Jackson relation (FJR; Faber & Jackson 1976), which relates the luminosity of a galaxy to its stellar velocity dispersion.

The highest quality and best understood scaling relations in the optical/near-infrared are the ones for early-type galaxies. This is because observationally they are much simpler than spirals, with less complicated star formation histories (SFHs), and less extinction by dust, and thus tighter scaling relations (e.g. Laurikainen et al. 2010). It is for this reason that often the two groups are treated separately in physically similar relations: the prime example being the relations between the central stellar velocity dispersion and absolute luminosity of elliptical galaxies (FJR), and the rotation velocity and absolute luminosity of disc galaxies (Tully & Fisher 1977). In an attempt to unify properties of these two groups, spiral galaxies are usually studied in terms of their bulge and disc properties. The resemblance of bulges to ellipticals has led to their inclusion in the scaling relations of early-type systems (e.g. Bender, Burstein & Faber 1992; Khosroshahi et al. 2000; Falcón-Barroso, Peletier & Balcells 2002), although they often reveal a much larger scatter and show, on average, an offset with respect to the relations of early-type galaxies. While this might not be surprising due to the mentioned effects of (younger) stellar populations and dust, part of the reason might also be the (often far from trivial) decoupling of the bulge from the disc.

These scaling relations exist for galaxy parameters at various radii. While photometric quantities inside one effective radius are easy to measure, the inherent limitations of traditional (single-aperture or long-slit) spectrographs have restricted the measurement of the stellar velocity dispersion to the central regions of galaxies. For instance, papers based on the Sloan Digital Sky Survey data

(Bernardi et al. 2003a, hereinafter B03; Graves & Faber 2010) use velocity dispersions that have been determined from central galaxy apertures, corrected to effective velocity dispersions using standard aperture corrections. In this paper, we follow the approach of Cappellari et al. (2006, hereinafter Paper IV) and make use of the panoramic capabilities of SAURON to measure velocity dispersions in circular apertures going out to an effective radius ($\sigma_{\rm e}$), and present scaling relations for which all the parameters are measured within the same aperture. This method offers the interesting possibility of presenting the spiral Sa galaxies in the same relations as early-type E/S0 galaxies. When measuring $\sigma_{\rm e}$ from the integrated galaxy spectrum, galaxy broadening can be caused by intrinsic velocity dispersions, or by galaxy rotation. Despite this uncertainty, $\sigma_{\rm e}$ will still be a measure of the mass in a galaxy inside $R_{\rm e}$. In addition, these velocity dispersions will not be affected by the presence of central discs, which often show low velocity dispersions (e.g. Falcón-Barroso et al. 2003). Since $R_{\rm e}$ for most of our Sa galaxies is much larger than the radius inside which the galaxy bulge dominates, the scaling relations will give us information about both the bulges and the inner discs of the Sa galaxies. This paper tends to investigate both issues by combining photometry with integral-field spectroscopy for a representative sample of E to Sa galaxies, treated in a consistent manner with a homogeneous data base and methods. The importance of this last point should not be overlooked, as supposedly standard parameters can vary greatly when measured by different groups. An example of this is provided by the measurement of nuclear cusp slopes (e.g. Ferrarese et al. 1994; Byun et al. 1996; Gebhardt et al. 1996; Carollo et al. 1997; Rest et al. 2001).

With these goals in mind, we have carried out an optical spectroscopic survey of 72 representative nearby E/S0 galaxies and Sa galaxies to $1R_{\rm e}$, using the custom-designed panoramic integral-field spectrograph SAURON mounted on the William Herschel Telescope, La Palma (Bacon et al. 2001, hereinafter Paper I). The SAURON representative sample was chosen to populate uniformly M_B–ϵ planes, equally divided between cluster and field objects (de Zeeuw et al. 2002, hereinafter Paper II). The work in this paper builds on previous results of our survey on scaling relations in other wavelength domains (Paper IV; Jeong et al. 2009, hereinafter Paper XIII). The reader is referred to other papers of the SAURON survey for results on the stellar kinematics (Emsellem et al. 2004) and kinematic classification (Cappellari et al. 2007; Emsellem et al. 2007) of early-type galaxies and their stellar populations (Kuntschner et al. 2006, 2010; Shapiro et al. 2010) and on the kinematics (Falcón-Barroso et al. 2006) and population of early spirals (Peletier et al. 2007). Hereinafter, we will refer to them as Paper III, X, IX, VI, XVII, XV, VII and XI, respectively.

We present in this paper homogeneous ground-based V-band and *Spitzer* 3.6-μm-band imaging observations of the 24 elliptical E, 24 lenticular S0 and 24 spiral Sa galaxies of the SAURON representative sample. Aperture photometry (growth curve analysis) is carried out to homogeneously derive a number of characteristic quantities to which the more complex SAURON integral-field observations are compared. We introduce the sample selection, biases and completeness in Section 2. The observations and basic data reduction are presented in Section 3. We describe the aperture photometry and determination of the spectroscopic quantities in Sections 4 and 5. Bivariate scaling relations are shown in Section 6, while the FP relation is specifically addressed in Section 7. We summarize our results and conclude briefly in Section 8. Descriptions of the stellar population synthesis models and methods used to derive stellar mass-to-light ratios for our galaxies are presented in Appendices A and B, respectively. Scaling relations showing the dependencies with kinematic substructure and environment are shown in Appendix C. Tables with the measured quantities are presented in Appendix D.

Throughout this paper, we adopt the *Wilkinson Microwave Anisotropy Probe* cosmological parameters for the Hubble constant, the matter density and the cosmological constant of, respectively, $H_0 = 73\,{\rm km\,s^{-1}\,Mpc^{-1}}$, $\Omega_{\rm M} = 0.24$ and $\Omega_{\rm L} = 0.76$ (Spergel et al. 2007), although these parameters have only a small effect on the physical scales of the galaxies due to their proximity.

2 SAMPLE SELECTION, BIASES AND COMPLETENESS

The SAURON sample is designed to be representative of the population of early-type galaxies in the nearby Universe. By construction, E, S0 and Sa galaxies were selected in equal numbers (24 in each group) to populate uniformly the absolute magnitude versus ellipticity diagram. Within each morphological class, galaxies were chosen to sample the field and cluster environments equally (12 in the field and 12 in clusters). The sample therefore consists of 72 galaxies. The basis for the sample selection was the Lyon/Meudon Extragalactic Database (Paturel et al. 1997).

Besides the astrophysically motivated criteria, the instrument specifications impose further constraints on the sample selection: $6^\circ < \delta < 64^\circ$ to avoid instrument flexure; $cz \leq 3000\,{\rm km\,s^{-1}}$ to ensure that all the lines of interest are in the observed spectral range; $M_B \leq -18$ mag to ensure that all central velocity dispersions (above 75 ${\rm km\,s^{-1}}$) can be measured; and $|b| \geq 15^\circ$ to avoid crowded fields and large Galactic extinctions. These restrictions make the SAURON set a representative but incomplete luminosity- and volume-limited sample of galaxies (see Paper II).

In Fig. 1, we show some of the main properties of the SAURON sample in the V and 3.6-μm bands. The photometric quantities have been derived as outlined in Section 4. The field-of-view (FoV) for a single pointing of the SAURON integral-field unit is $33 \times 41\,{\rm arcsec}^2$ and therefore, as shown in the figure, covers up to 1 effective (half-light) radius, $R_{\rm e}$, for most of our galaxies. Larger galaxies were usually mosaiced with several SAURON pointings to reach the effective radius. As intended in our sample selection, our galaxies uniformly populate the desired absolute magnitude range above the selection cut.

While Fig. 1 illustrates the limits in size, mean surface brightness and luminosity of our sample, it still lacks information about potential biases (other than the luminosity) and the level of completeness of our sample. Preliminary checks with larger, more complete samples of early-type galaxies (B03; La Barbera et al. 2010; Cappellari et al. 2011) reveal that our SAURON representative sample covers rather well the parameter space defined by these three photometric indicators for $\langle\mu_{\rm e}\rangle \lesssim 21\,{\rm mag\,arcsec^{-2}}$ at the V band. We illustrate this using the g-band catalogue of B03 as a comparison sample in Sections 6 and 7. This data set consists of around 9000 early-type galaxies up to redshift 0.3 with stellar velocity dispersions above $70\,{\rm km\,s^{-1}}$.

3 OBSERVATIONS AND DATA REDUCTION

3.1 MDM data set

Part of the imaging data were obtained at the 1.3m McGraw-Hill Telescope of the MDM Observatory located on Kitt Peak, Arizona, over five observing runs totalling 40 nights: 2003 March 25–April 6, 2003 October 27–November 2, 2004 February 18–25, 2005 April

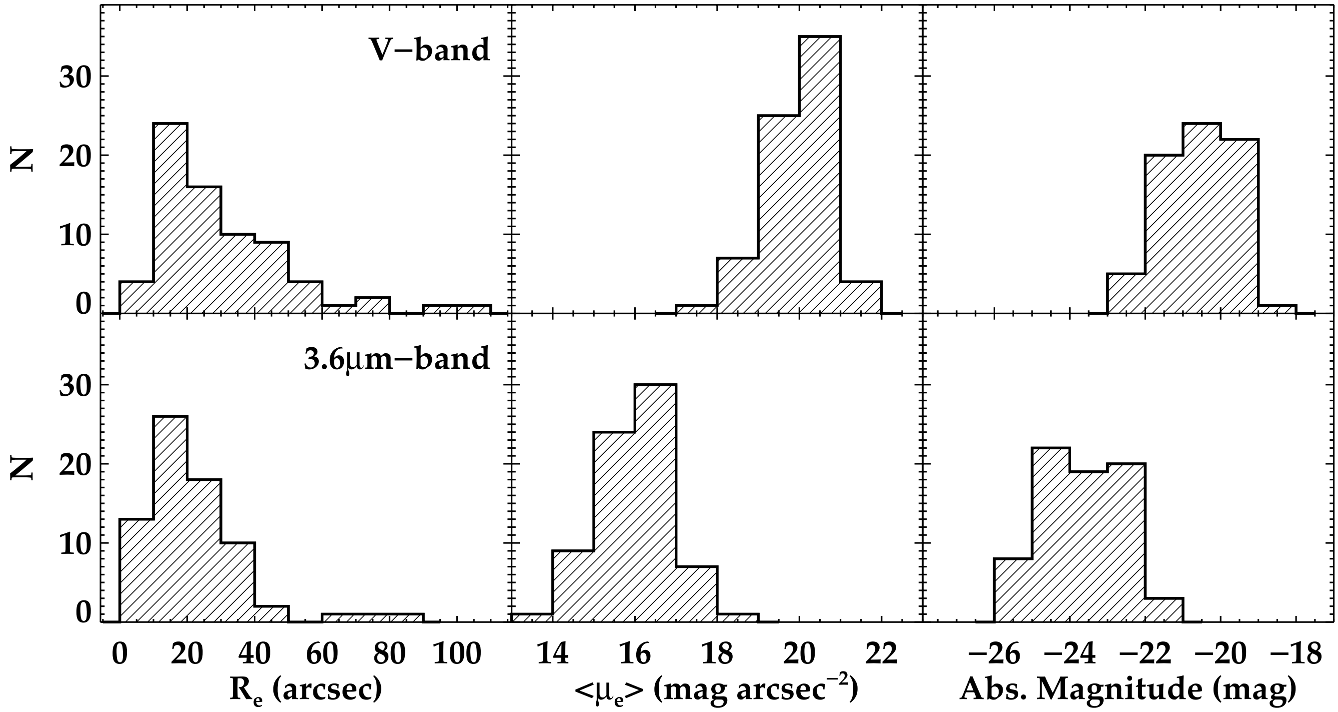

Figure 1. Photometric characterization of the SAURON survey. Top row: V-band effective radius (R_e), mean effective surface brightness ($\langle\mu_e\rangle$) and absolute total magnitudes. Bottom row: same quantities in the 3.6-μm band from the *Spitzer*/IRAC data set. The sample is defined such that galaxies uniformly populate the desired (B-band) absolute magnitude range and that our integral-field observations reach typically as far as $1R_e$ (see Paper II).

11–17 and 2005 November 2–6. The entire SAURON representative sample was observed (Paper II). The thin 2048 × 2048 pixel^2 backside-illuminated SITE 'echelle' CCD was used, and an additional 128 column virtual overscan region was simultaneously obtained with every frame. In direct imaging mode (f/7.5), this yields pixels of 0.508 × 0.508 arcsec^2 and a 17.4 × 17.4 arcmin^2 FoV, ensuring proper sampling of the seeing and plenty of sky around the targets for sky subtraction. The seeing was typically 1.8–2.6 arcsec and no observation with a seeing above 3.0 arcsec was used. The readout noise and gain were typically 3.0 and 5.7 e$^-$ ADU^{-1}, respectively. The *Hubble Space Telescope* (*HST*) $F555W$ and $F814W$ filters were used, similar to the Cousins V and I optical filters. Long non-photometric exposures were obtained during most nights. To reach a sufficient depth and allow for correction of CCD defects when combining the images, our stated goal was to acquire at least three long offset exposures in each filter for every object. Exposure times for individual long exposures were typically 400 s in $F555W$, although we adjusted both the exposure times and the number of exposures based on weather conditions. To internally calibrate the photometry, we also acquired a short (100 s) exposure of every object during the few truly photometric nights.

3.1.1 Data reduction

The data reduction of the MDM images was carried out using standard procedures in IRAF.[1] The bias was subtracted in two steps. First, the average of the overscan region of each frame was subtracted from each column. Secondly, a 'master' bias was subtracted from every frame. Since the bias was found to be stable, we used a run-wide average of (overscan-subtracted) bias frames obtained at the beginning and end of each night. Dark current was found to be non-negligible and was subtracted using a 'master' dark, again resulting from a run-wide average of dark frames obtained at night during bad weather conditions. All galaxy and standard star exposures were then divided by a 'master' flat-field frame, resulting from an average of twilight frames obtained in each filter. Surprisingly, the flat-fields were found to vary from night to night by up to 2 per cent, so a night average was used whenever possible. This is not a major limitation, however, as we are mostly interested in azimuthally averaged quantities (see Section 4). All images of a given galaxy in each filter were registered using the MATCH routine by Michael Richmond (available at http://spiff.rit.edu/match/), based on the algorithm by Valdes et al. (1995). Star lists were obtained using SEXTRACTOR (Bertin & Arnouts 1996). Position uncertainties in the registered images were typically smaller than a tenth of a pixel. Individual images were then sky-subtracted and combined using a sigma clipping algorithm and proper scaling. Independently of the photometric calibration, the short exposures are essential in the central region of many objects, where long exposures are often saturated. The combined images were flux-calibrated using the photometric transformations determined, night by night, in the way explained below. We estimate the limiting surface brightness of our V-band data (≈25 mag arcsec^{-2}) as the surface brightness level 1σ above the uncertainties in the determination of the sky.

3.1.2 F814W images

During the reduction of the data, a few important issues were identified in the $F814W$ images. First, the images suffered from

---

[1] IRAF is distributed by the National Optical Astronomy Observatories, which is operated by the Association of Universities for Research in Astronomy, Inc., under cooperative agreement with the National Science Foundation, USA.

fringing at the 1–2 per cent level. Since no night-time exposure of blank fields was obtained, we attempted to devise an alternative correction from standard star exposures, and also from the galaxies' exposures themselves. Standard star images, however, proved to have too low signal-to-noise ratios (S/Ns), while median-combined galaxy exposures failed to remove all the galaxy signal, as most of our targets cover a substantial fraction of the FoV. We therefore could not correct for the fringing. Secondly, and most importantly, stars in the $F814W$ long-exposure images showed a faint, but extended halo around them. This was mostly notable in the saturated stars. This problem, commonly termed 'red halo point spread function (PSF)', is due to the use of thinned CCDs together with other effects related to the ageing of the telescope coating (see Michard 2002 for an in-depth study on the issue). These cause the PSF in the $F814W$ filter to extend to well over 100 arcsec (see also Wu et al. 2005; de Jong 2008). Although one could in principle devise a correction, it would be rather uncertain. Since this issue will affect any measurement with this filter, we deemed the $F814W$ data set unreliable and discarded it from our analysis.

The effective radii presented in previous papers of the SAURON series [Papers IV, VI, IX, X, McDermid et al. 2006 (hereinafter Paper VIII) and Scott et al. 2009 (hereinafter Paper XIV)] were computed from combined $F814W$ *HST* and MDM images before we identified this issue. Nevertheless, the values calculated there appear to be 1 per cent smaller than the ones measured here in the V band (thus consistent with the presence of colour gradients) and with a scatter implying a small error of 8 per cent. Note that this issue has no effect on any of the conclusions in those papers and has a very small effect on the quantities derived from our integral-field data, which have been updated in Paper XV and subsequent papers of the SAURON series.

3.1.3 *Flux calibration*

During photometric nights, in addition to galaxies, we also performed repeated observations of stellar fields including standard stars from Landolt (1992), covering a range of apparent magnitudes and colours; for many fields, the observations were repeated at the beginning, in the middle and at the end of the night, in order to also calibrate the dependence on airmass. In total, we acquired 84 stellar fields, with several (three to ≈10) standard stars in each one. The aim was to calibrate the data using photometric solutions of the following form:

$$m_{V,\mathrm{std}} = m_{F555W,\mathrm{ins}} + z_{F555W} + k_{F555W} A + c_{F555W}\,(m_{V,\mathrm{std}} - m_{I,\mathrm{std}}), \quad (1)$$

where m_{std} are the standard magnitudes from Landolt (1992), m_{ins} is the instrumental magnitude, z is the photometric zero-point, k is the atmospheric extinction coefficient, A is the airmass and c is the colour-correction coefficient. In practice, for each of our stellar fields, we identified the standard stars with the help of the maps published by Landolt (1992), and for each star measured the magnitude which enters in equation (1) as m_{ins}. This was done by means of standard IRAF tasks, within the *noao.digiphot.daophot* and *noao.digiphot.photcal* packages. The sky background was evaluated taking the mode of the intensity in an annular region around each star, situated three to four times the full width at half-maximum (FWHM) of the stellar profile away from its peak; the star was sky-subtracted and the computed magnitude corrected for aperture effects. All the stars affected by scattered light or saturated, and those for which the fits performed in IRAF did not converge, were removed. We took all the remaining stars with measured instrumental magnitudes and solved equation (1) for z, k and c. We then grouped the stars according to the night in which they had been observed and solved again equation (1) on a 'per-night' basis, keeping the colour term c – which is very close to zero – fixed to the 'global' value determined in the previous step and fitting for the airmass term k and the zero-point z only. Given that the standard magnitudes of the reference Landolt stars are in the V band (Johnson) filter, the photometry of our images is based on that filter. During the flux calibration, we have therefore converted our images from the *HST* $F555W$ to the V-band (Johnson) filter.

The internal accuracy of our flux calibration is around 0.03 mag. In order to investigate systematic departures of our calibration, we compared our measurements to apparent magnitudes measured with the same aperture on *HST*/WFPC2 PC1 images. The set of galaxies used in the comparison is that published by Lauer et al. (2005) and for which sky values are reported. The choice of aperture was arbitrarily set to $R_{\mathrm{e}}/2$, with the constraint of it being larger than 5 arcsec to avoid uncertainties derived from the different PSFs and smaller than 15 arcsec to be fully included within the PC1 chip. The difference between our V-band magnitudes and those of Lauer's *HST*/$F555W$ imaging is better than 0.05 mag rms, with a small systematic offset. The MDM flux calibration predicts slightly brighter ($\lesssim$0.05 mag) galaxies than the *HST*. This shift is, however, within the expected $V - F555W$ zero-point transformation for different late-type stellar templates (i.e. it conforms to the dominant old population in our galaxies).[2]

3.2 *Spitzer*/InfraRed Array Camera 3.6-μm data set

In an attempt to extend our analysis of the scaling relations to longer wavebands than the optical, and to alleviate the loss of the $F814W$ MDM observations, we decided to use the homogeneous InfraRed Array Camera (IRAC) 3.6-μm imaging data set provided by the *Spitzer* telescope. This data set has the great advantage of being less sensitive to the presence of dust and provides a better tracer for the underlying, dominant, predominantly old stellar mass component of galaxies.

We retrieved the IRAC images of our sample galaxies at 3.6 μm through the Spitzer Science Center archive. These archival images cover a significant fraction of the SAURON sample and were acquired in the context of several programmes. The remaining objects were observed as part of the specific programme 50630 (PI: G. van der Wolk) during Cycle 5, meant to complete observations of the SAURON sample in both IRAC and Multiband Imaging Photometer for Spitzer bands. We used the BCD images and mosaiced them together using the MOPEX software. This avoided the artificial point sources sometimes present in the centre of the PBCD images. Details about the reduction are given in the IRAC Instrument Handbook.[3] The output mosaics were then sky-subtracted in the standard way. As indicated in the handbook, a zero-point of 280.9 Jy was assumed for flux calibration of the data into the Vega system. Further details regarding the data reduction can be found in Paper XV and in van der Wolk et al. (in preparation).

After the data reduction and flux calibration processes, we estimate the limiting surface brightness of our 3.6-μm-band data to be ≈21 mag arcsec^{-2}. In order to illustrate the quality of our imaging,

---

[2] See table 5.2 in the *HST*/WFPC2 handbook for zero-point transformations (http://www.stsci.edu/hst/wfpc2).

[3] http://ssc.spitzer.caltech.edu/irac/dh/

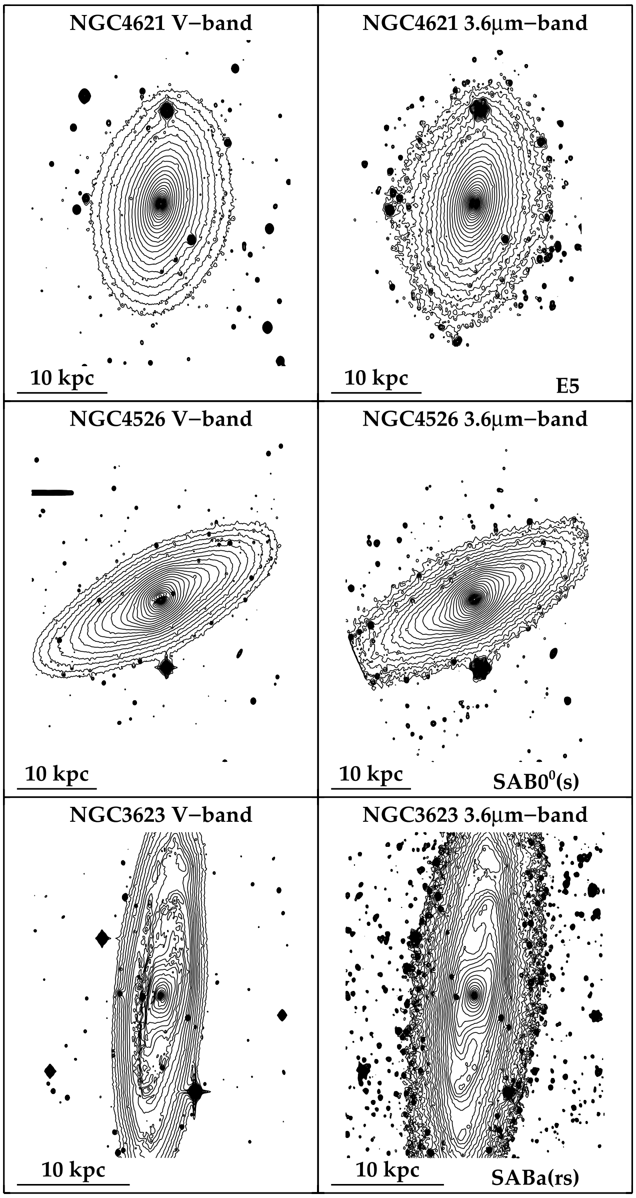

Figure 2. Contours of the surface brightness of three galaxies in the SAURON sample (in steps of 0.25 mag arcsec^{-2}) in both the V and 3.6-μm bands. The largest isophotes are set to reach the limiting surface brightness of the survey in each band ($\approx$25 and $\approx$21 mag arcsec^{-2}, respectively). The orientation of the images is such that north is up and east is left. The Hubble morphological type is indicated in the bottom right-hand corner. The FoV of the observations is much larger than displayed here.

in Fig. 2, we show isophotal contours down to the limiting surface brightness of a few galaxies in our sample. The consistency in the photometric depth of both data sets ensures that our measured parameters truly reflect the potential structural changes as a function of waveband, and are not affected by poor imaging.

3.3 Distances

We have made a comprehensive effort to collect the best available distance estimates in the literature for all galaxies in our sample. We have assigned distance estimates adopting the following priority order in the methods used:

(i) For 42 galaxies, the distances were obtained with the surface brightness fluctuation method by Mei et al. (2007) for the ACS Virgo Cluster Survey, by Cantiello et al. (2007) using archival ACS imaging and by Tonry et al. (2001) using ground-based imaging. We subtract 0.06 mag from the latter distance moduli (i.e. a 2.7 per cent decrease in distance) to convert to the same zero-point as the HST Key Project Cepheid distances (Freedman et al. 2001).

(ii) For one galaxy (NGC 5308), the distance is derived using Type Ia supernova luminosities from Reindl et al. (2005), subtracting 0.43 mag from the distance moduli to convert to $H_0 = 73\,\mathrm{km\,s^{-1}\,Mpc^{-1}}$.

(iii) For 10 galaxies within 12° of the Virgo Cluster centre (defined by the galaxy M87) and with heliocentric velocities $< 2500\,\mathrm{km\,s^{-1}}$, we followed Crook et al. (2007) and assigned the Virgo Cluster distance modulus of 31.092 mag (Mei et al. 2007) and an error of 0.082 mag due to the depth of the cluster.

(iv) For two galaxies (NGC 2273 and 5448), the distances are based on 'look-alike' galaxies (Paturel 1984) from Terry, Paturel & Ekholm (2002), calibrated with the HST Key Project Cepheid distances.

(v) For four galaxies, the distances are based on the correlation between galaxy luminosity and linewidth (Tully–Fisher relation) from Tully et al. (2008), calibrated with the HST Key Project Cepheid distances.

(vi) For one galaxy (NGC 5198), the distance is based on the D_n–σ (see Dressler et al. 1987) relation from Willick et al. (1997), adopting $H_0 = 73\,\mathrm{km\,s^{-1}\,Mpc^{-1}}$ and an error of 0.40 mag in the distance modulus.

(vii) For the remaining 12 galaxies, the distances are based on their observed heliocentric radial velocities given by the NASA/IPAC Extragalactic Database (NED),[4] using the velocity field model of Mould et al. (2000) with the terms for the influence of the Virgo Cluster and the Great Attractor.

Methods (i)–(iii) typically yield errors in the distances of $\lesssim$10 per cent, while methods (iv)–(vi) are expected to be accurate to better than $\lesssim$20 per cent. Comparing these reliable distance estimates for 60/72 galaxies in our sample with the distance estimates based on the observed redshifts using method (vii), we find a (biweight) dispersion of $\approx$23 per cent. Taking into account the average 7 per cent error in the accurate distance estimates, we thus adopt for the redshift distances a typical error of $\approx$22 per cent, that is, 0.487 mag in the redshift distance modulus. Tables D1 and D2 list the adopted distances as well as the sources of the distance estimates.

4 PHOTOMETRIC QUANTITIES

One of the main goals of this project is the measurement of homogeneous photometric quantities. As in Paper IV, we have opted for simple, yet frequently used, methods to derive these values. This has the advantage of being well reproducible and of allowing comparison with a wide range of studies (e.g. Burstein et al. 1987; Jørgensen, Franx & Kjaergaard 1992). The values measured here are based on aperture photometry. For each galaxy, in both the V band and the 3.6-μm band, we extracted radial profiles on circular apertures using the MGE_FIT_SECTORS IDL[5] package of Cappellari (2002). Foreground stars and nearby objects were masked using the SEXTRACTOR lists generated for the registration of the images (see Section 3.1.1). The profiles were flux calibrated and corrected

---

[4] http://nedwww.ipac.caltech.edu/

[5] http://www.ittvis.com/

for Galactic extinction using the A_V and $A_{3.6\,\mu\mathrm{m}}$ values from the NED, which are based on *COBE*, *IRAS* and the Leiden–Dwingeloo H I emission maps as discussed by Schlegel, Finkbeiner & Davis (1998). We have made no attempt to correct the observed fluxes or luminosities for internal extinction.

In all the figures of this paper, the circles denote E/S0 galaxies and the diamonds denote Sa galaxies. The filled symbols indicate galaxies with good distance estimates, whereas the open symbols denote those with only recession velocity determinations. In blue, we highlight fast rotator galaxies, in red, slow rotator galaxies (see Section 5.1) and in green, Sa galaxies. The special case of NGC 4550, a galaxy known to consist of two counter-rotating stellar discs of similar mass (Rix et al. 1992; Paper X), is marked in yellow.

4.1 Effective radii, mean effective surface brightnesses and absolute magnitudes

We have determined the effective radii and mean effective surface brightnesses for our sample galaxies by fitting our aperture photometry profiles with $R^{1/n}$ (Sérsic 1968) growth curves of the form

$$\begin{aligned} L(<R) &= 2\pi \int_0^R I(R')R'\mathrm{d}R' \\ &= 2\pi n I_\mathrm{e} R_\mathrm{e}^2 \frac{\mathrm{e}^{b_n}}{(b_n)^{2n}} \gamma\left[2n, b_n(R/R_\mathrm{e})^{1/n}\right], \end{aligned} \tag{2}$$

with γ the incomplete gamma function, R_e the effective radius, I_e the effective surface brightness (at R_e), n the Sérsic index describing the curvature of the radial profile, and we adopt (Ciotti & Bertin 1999)

$$b_n = 2n - \frac{1}{3} + \frac{4}{405n} + \frac{46}{25515n^2}, \tag{3}$$

which is an approximation to better than 10^{-4} for $n > 0.36$.

When fitting the growth curve profiles, generally the inner ≈10 arcsec as well as regions outside 1σ above the sky level have been ignored. The former avoids potential complications due to the point spread function and the latter reduce the uncertainties associated with imperfect sky subtraction. We have used the integrated Sérsic profile only to extrapolate the outermost part of the growth curve to infinity and estimate the total galaxy luminosity. After this, we have determined R_e from the radius where the growth curve profiles are equal to half this total luminosity, that is, equal to $L_\mathrm{e} = L(<R_\mathrm{e})$. In other words, we have not adopted the R_e values from the Sérsic fit, even though they turned out to be very similar to those from the growth curve profiles after obtaining L_e from the Sérsic fit. While the surface brightness profiles of galaxies are not perfectly described by an $R^{1/4}$ law (e.g. Caon, Capaccioli & D'Onofrio 1993; Graham et al. 1996; MacArthur, Courteau & Holtzman 2003), the growth curves for the vast majority of the objects in our sample, typically early-type galaxies, were well represented at large radii by $n = 4$. However, the growth curves of galaxies displaying extended discs and intermediate to edge-on configurations (i.e. mainly spirals, but also some lenticulars) were often poorly described by a de Vaucouleurs law; hence, we fitted a Sérsic law with $n < 4$ instead. Overall, the adopted Sérsic indices n were the same in both the V band and the 3.6-μm band. The adopted Sérsic n values together with all the other photometric quantities for the sample galaxies are listed in Tables D1 and D2. The approach of using an $R^{1/4}$ growth curve to extrapolate the galaxy luminosity to infinity was the same as adopted by classic studies (e.g. Burstein et al. 1987; Jørgensen, Franx & Kjaergaard 1995) and by previous papers of our survey on scaling relations (e.g. Paper IV). This allows for a direct comparison of our numbers with theirs. In addition to the measurements of L_e and R_e, we have computed their uncertainties via Monte Carlo realizations. Besides including the uncertainty in the background sky subtraction, we included correlations among the pixels in the images in two different ways, providing lower and upper limits to the uncertainties. First, we assumed that the dominant source of error is Poisson noise and that the pixels are uncorrelated when we include the errors in the sky, except for scales smaller than the FWHM of the PSF. For those scales, we defined a correlation length (FWHM/pixel scale) which we set to 2.0 after some tests. The choice of this correlation length does not significantly change the output uncertainties for values below 6. Secondly, we assumed that the pixels are fully correlated and that this is significantly higher than the Poisson noise (which was also included). We adopted as the uncertainty the one produced by the first method, throughout this paper. The second estimate is a good test to assess the maximum error one could expect in the worst possible situation. For reference, we show the different error measurements for R_e in Fig. 3.

The total apparent magnitude and corresponding uncertainty follows from L_e, simply as $m = -2.5\log(2L_\mathrm{e})$. The mean effective surface brightness was computed by dividing L_e, the total luminosity measured within 1 effective radius, by the area of the aperture, $A_\mathrm{e} = \pi R_\mathrm{e}^2$, and expressing it in magnitudes, $\langle\mu_\mathrm{e}\rangle = -2.5\log(L_\mathrm{e}/A_\mathrm{e})$. Since the effective luminosity and radius are correlated, the uncertainty in the mean effective surface brightness was derived after first computing the $\langle\mu_\mathrm{e}\rangle$ values for each of the corresponding Monte Carlo realizations of L_e and R_e.

As already shown by other authors (e.g. Pahre 1999; B03; MacArthur et al. 2003; La Barbera et al. 2004), R_e values in the infrared appear to be, in general, smaller than those in optical bands. This is mostly due to the fact that galaxies tend to be bluer in the outer parts and therefore emit less light at these longer wavelengths (Peletier et al. 1990). In Fig. 3, we show the relation we find

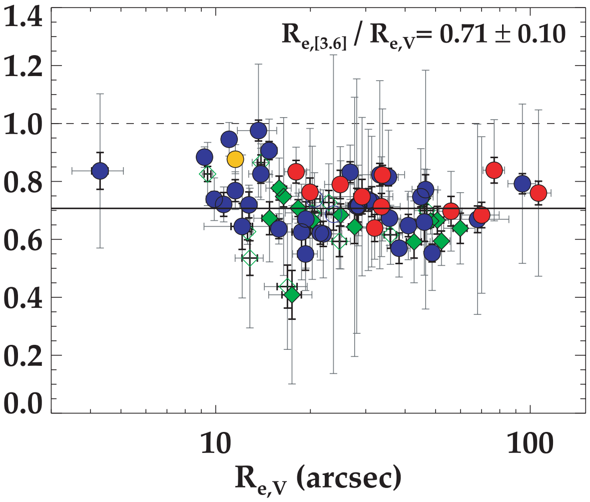

Figure 3. Ratio between $R_{\mathrm{e},V}$ and $R_{\mathrm{e},[3.6]}$ for our sample of galaxies. The solid thick line shows the average ratio ($R_{\mathrm{e},[3.6]}/R_{\mathrm{e},V}$). The dashed line marks the one-to-one relation. The circles denote E/S0 galaxies and the diamonds denote Sa galaxies. The filled symbols indicate galaxies with good distance estimates and open symbols indicate those with only recession velocity determinations. In blue, we highlight FRs, in red, SRs, and in green, the Sa galaxies. The special case of NGC 4550, with two similarly-massive counter-rotating disc-like components, is marked in yellow. The black/grey error bars denote the minimum/maximum uncertainties in our analysis (see Section 4.1).

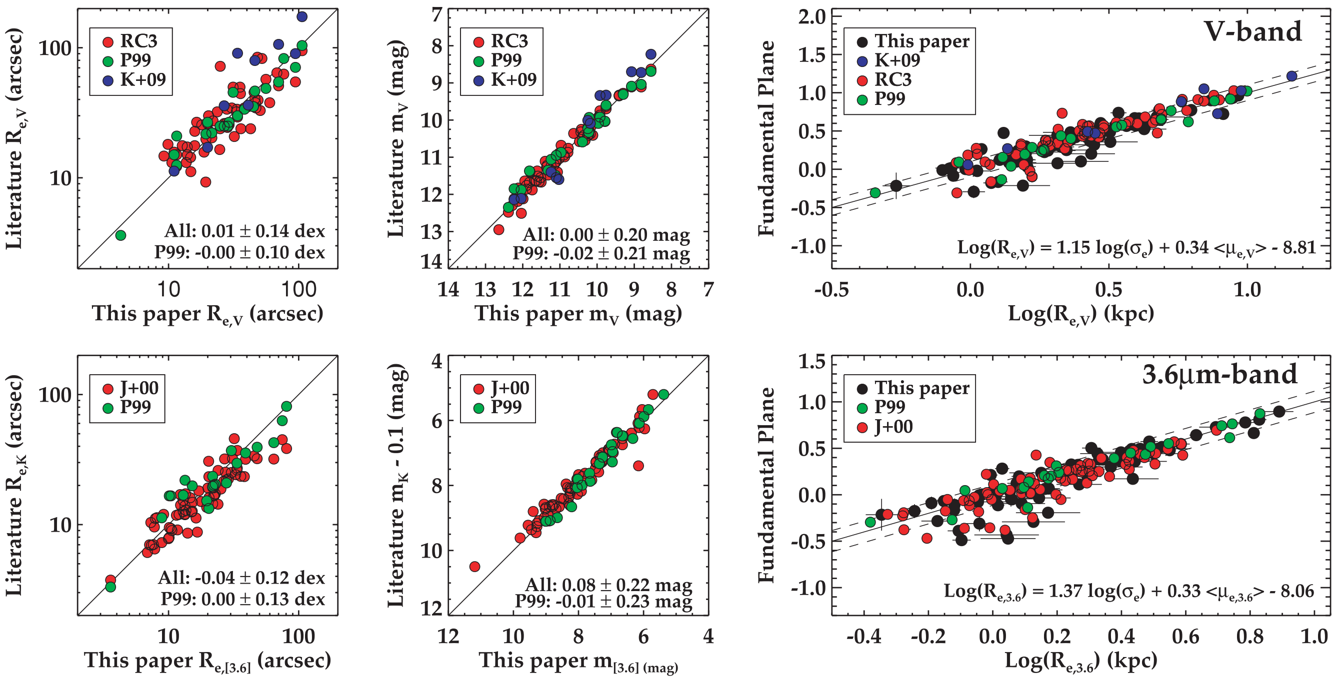

Figure 4. Comparison of our aperture photometry with the literature. Four leftmost panels: R_e and apparent magnitudes from this paper are compared to those in the literature (RC3, de Vaucouleurs et al. 1991; P99, Pahre 1999; J+00, Jarrett et al. 2000; K+09, Kormendy et al. 2009) for the V and 3.6-μm bands. We subtracted 0.1 mag from the literature K-band values (i.e. the mean $K - [3.6]$ colour for old stellar populations) to compensate for the colour difference. Mean offset and scatter are indicated for all sources (All) and P99 alone (as it is the only sample available in the two bands for the two quantities). Two rightmost panels: the best FP relations derived in Section 7.1 showing our data as well as the literature data for our sample of galaxies (see details in Section 4.2). The dashed lines in the FP relations mark the 1σ uncertainty.

between the independently measured $R_{e,V}$ and $R_{e,[3.6]}$ values; $R_{e,[3.6]}$ is on average 29 per cent smaller than $R_{e,V}$. As a results of this, and as shown in Sections 6 and 7, differences are thus found in the scaling relations for the two photometric bands.

4.2 Literature comparison

In order to test the reliability of our measurements, we have compared them with published values in the literature. This exercise can reveal large differences among sources, mainly depending on the depth of the data, photometric band and most importantly the methodology used to derive the relevant quantities. In Fig. 4, we show the comparison of our estimated values with a few references in the literature (de Vaucouleurs et al. 1991; Pahre 1999; Jarrett et al. 2000; Kormendy et al. 2009). When necessary, the literature major-axis R_e estimates have been transformed to the geometric-mean radius to compare with our values obtained from circular apertures. As shown in the figure, the agreement with the different sources is generally good with a typical scatter of about 0.14 dex in R_e and 0.2 mag in apparent magnitude. The most notorious difference in our sample is that of NGC 4486 (M87), where our measured value in the V band of 106 arcsec contrasts with other values in the literature (95 arcsec, de Vaucouleurs et al. 1991; 104 arcsec, Pahre 1999; 171 arcsec, Ferrarese et al. 1994; 194 arcsec, Kormendy et al. 2009).

In addition, we show the best-fitting FP relations presented in Section 7.1, including data from the same sources. We carry out this comparison to assess whether different methods to estimate the structural parameters can affect our relations. In order to minimize uncertainties, we have re-derived σ_e for each source's R_e value. In addition, if not provided, our estimated distances were used to convert R_e from arcsec to kpc. In the case of Kormendy et al. (2009), we do not use their tabulated mean surface brightnesses, but instead compute them ourselves from the total luminosity and effective radii they provide in their table 1 (columns 9 and 17). This is to mimic as much as possible our procedure to compute the photometric quantities. The figure shows that even though the structural parameters individually might vary between different sources, in combination, they agree well within the observed scatter, and thus our best-fitting parameters should not be biased in any particular way.

4.3 $V - [3.6]$ colours

Colour measurements have been widely used in the past to extract first-order information on the stellar content of galaxies and constrain different formation scenarios (e.g. White 1980; Carlberg 1984). Here we determine the effective colour

$$(V - [3.6])_e = -2.5 \log[L_V(< R_{e,V})/L_{[3.6]}(< R_{e,V})] + \text{constant} \tag{4}$$

measured within an $R_{e,V}$ aperture. The choice of $R_{e,V}$ was preferred over $R_{e,[3.6]}$ to match the aperture used to extract our SAURON spectroscopic quantities (see Section 5). Aperture corrections, as devised in the IRAC Instrument Handbook, have been taken into account when deriving the colours. We will use the information from these parameters, together with absorption line-strength indices, to establish the stellar population properties of our galaxies in different regions of the scaling relations presented here.

Central colours (e.g. within $R_{e,V}/8$) were not derived due to the complexity in matching the MDM and *Spitzer* PSFs. Furthermore, $V - [3.6]$ colour gradients were also discarded, given the presence of dust in many of our galaxies, which introduces features in the colour profiles that cannot be accounted for with a single linear relation. Nevertheless, an in-depth analysis of colour profiles in the SAURON sample, using the *Spitzer*/IRAC 3.6- and 4.5-µm bands, will be the subject of study in Peletier et al. (in preparation).

5 SAURON QUANTITIES

In addition to the aperture photometry extracted from the MDM and *Spitzer*/IRAC images, we have determined a number of quantities from our SAURON integral-field data that are key for the analysis presented in this paper. These are parameters describing the richness in dynamical substructures and the stellar content of the galaxies in our sample. They have been computed following the procedures detailed in previous papers of the SAURON survey. Here we will briefly summarize the main aspects and refer the reader to the relevant papers for a full description of the methods employed. For convenience, the final set of spectroscopic quantities are listed in Tables D3 and D4.

5.1 Kinematic quantities

The stellar kinematics of our sample galaxies have been extracted following the procedure outlined in Papers IX and X. Briefly, we used PPXF (Cappellari & Emsellem 2004) to fit a linear combination of stellar templates from the MILES library (Sánchez-Blázquez et al. 2006b) and derive the best mean velocity V and velocity dispersion σ for each spectrum in our data cubes. In this paper, we are mostly interested in extracting the true first two velocity moments of the line-of-sight velocity distribution, and therefore we deliberately do not fit the higher order moments (h_3, h_4). We use the extracted V and σ maps to compute λ_R, a parameter that measures the specific angular momentum within $R_{\mathrm{e},V}$ and that has led to the new kinematical classification of galaxies presented in Paper IX. Throughout this paper, we will identify as *slow rotators* (hereinafter SRs) those galaxies with $\lambda_R \leq 0.1$ and as *fast rotators* (hereinafter FRs) the rest (as in all the papers in the SAURON series since Paper IX). We note that for this sample, the notation is consistent with that based on the improved criterion defined in Emsellem et al. (2011) for the galaxies in the ATLAS$^{\mathrm{3D}}$ sample[6] (Cappellari et al. 2011).

In order to plot some of the scaling relations given in Section 6, we have measured the mean stellar velocity dispersion within an $R_{\mathrm{e},V}$ aperture. For that purpose, we summed up all the spectra available within such a *circular* aperture and then computed σ following the same procedure as described above. Whenever the aperture was not fully contained within the SAURON FoV, we used the velocity dispersion calibration of Paper IV (equation 1) to correct our values. For some aspects in Section 7.5, we have also measured the mean stellar velocity dispersion within an $R_{\mathrm{e},V}/8$ aperture ($\sigma_{\mathrm{e},8}$). As in other papers in the survey (see Papers IV and XVII), we adopt a random error of 5 per cent for our measured velocity dispersion values.

Finally, we make use of the results in Krajnović et al. (2008, hereinafter Paper XII) to describe the level of kinematic substructure present in our maps (e.g. inner discs, kinematically decoupled cores, kinematic twists).

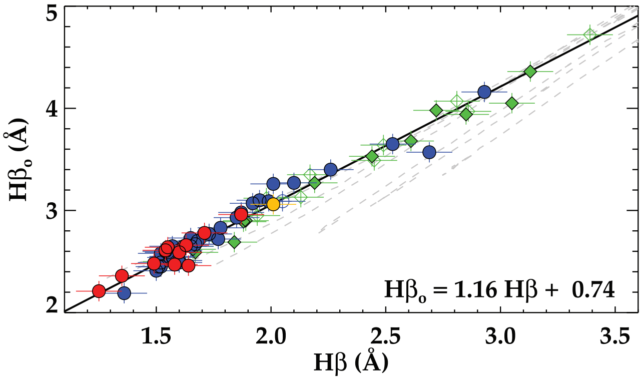

Figure 5. Relation between the Hβ and Hβ_0 line-strength indices for our sample galaxies. Colours and symbols are as in Fig. 3. The dashed grey lines mark the predictions of the VAZ10 models for different metallicities. ([M/H] = [−2.32, −1.71, −1.31, −0.71, −0.40, 0.0, +0.2]). Our sample appears to closely follow the predictions at high metallicities.

5.2 Stellar population quantities

As well as stellar kinematic quantities, we have also measured line-strength indices within $R_{\mathrm{e},V}$. In this paper, in order to be fully consistent with the procedures employed to derive the stellar kinematics and to minimize the uncertainties in the absolute calibration of the line-strength indices, we have opted to measure the indices in the recently defined *Line Index System* (LIS) LIS-14.0 Å (Vazdekis et al. 2010, hereinafter VAZ10). This method has the advantage of circumventing the use of the so-called Lick fitting functions for the model predictions, which requires the determination of often uncertain offsets to account for differences in the flux calibration between models and observations. The only required step to bring our flux-calibrated data to the LIS-14.0 Å system is to convolve the aperture spectra to a total FWHM of 14.0 Å. The choice of LIS-14.0 Å over other proposed systems (e.g. LIS-5.0 Å or LIS-8.4 Å) is imposed by the galaxy with the largest σ_{e} in our sample (i.e. NGC 4486).

Besides the standard Lick indices (Worthey 1994) that can be measured within our wavelength range (i.e. Hβ, Fe5015, Mg*b*), we have also measured the Hβ_0 index presented in Cervantes & Vazdekis (2009). This new index is similar to the classical Hβ index, but it has the advantage of being less sensitive to metallicity. For convenience, we show the relation between the two indices for our galaxies in Fig. 5. We, however, warn the reader that this relation is necessarily biased by our sample selection. Since we are using stellar population models with solar abundance ratios, we use the [MgFe50]′ index[7] to minimize the effects of α-elements over abundances (see Paper XVII). For galaxies with $R_{\mathrm{e},V}$ larger than the SAURON coverage, we applied the line-strength aperture corrections devised in Paper VI. As established in Paper XVII, typical random errors for our measured values are 0.1 Å, with systematic uncertainties being 0.06, 0.15 and 0.08 Å for Hβ, Fe5015 and Mg*b*, respectively. We assume the same aperture corrections and errors as Hβ for the Hβ_0 index.

Fig. 6 shows the location of our galaxies in the Hβ and Hβ_0 versus [MgFe50]′ diagrams in the LIS-14.0 Å system. The figure illustrates the main reasons for adopting the Hβ_0 index over the traditional Lick Hβ index: (1) Hβ_0 is more insensitive to metallicity than Hβ down to [M/H] ≈ −0.71, which makes the diagram more

---

[6] http://purl.org/atlas3d

[7] $[\mathrm{MgFe50}]' = 0.5 \times [0.69 \times \mathrm{Mg}b + \mathrm{Fe5015}]$.

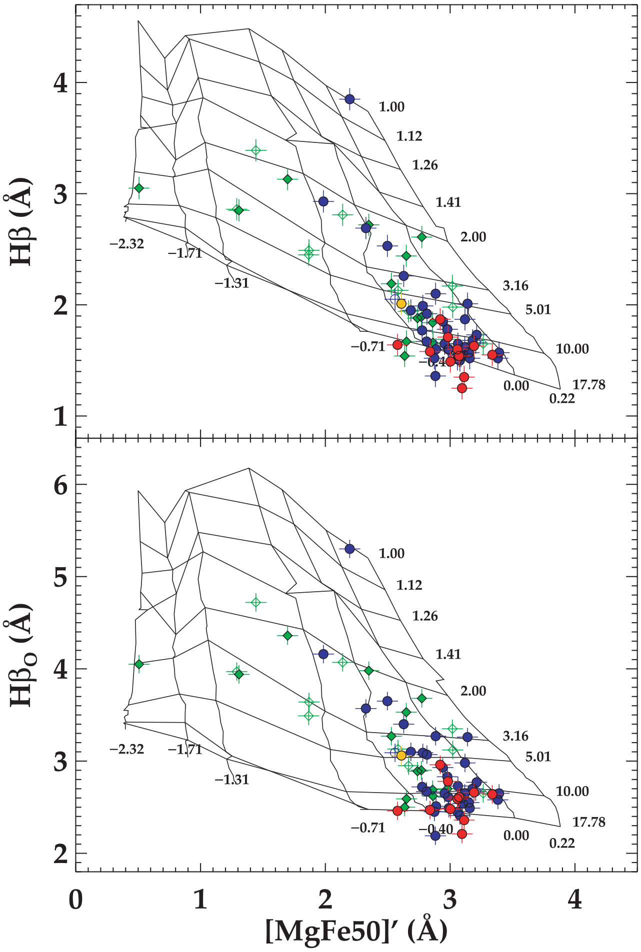

Figure 6. Line-strength index relations for the SAURON sample galaxies in the LIS-14.0 Å system (VAZ10). Colours and symbols are as in Fig. 3. The line-strength indices presented have been measured within an $R_{\mathrm{e},V}$ aperture. Grids show model predictions for constant ages (horizontal lines with labels in Gyr) and metallicities (vertical lines labelled with [M/H] with respect to solar metallicity). The top panel shows the classical Hβ Lick index (Worthey 1994) versus [MgFe50]′. The bottom panel shows the same diagram, but with the recently defined Hβ_0 index (Cervantes & Vazdekis 2009) instead of Hβ.

orthogonal; and (2) the vast majority of our galaxies fall within the model predictions, which is crucial for a proper estimation of the stellar mass-to-light ratios (γ_*).

Throughout this paper, we investigate the potential dependencies on age via the line-strength index Hβ_0. This is to be able to include the Sa galaxies in the same diagrams. While the use of ages, metallicities and abundance ratios is in general desired, estimates of these parameters from a single-stellar population (SSP) analysis, as was done for the 48 E and S0 galaxies in Paper XVII, are not recommended, given the more continuous star formation activity they have experienced (see Paper XI for more details on these and other caveats). The use of the Hβ_0 index will instead provide a robust first-order indication of the presence of young stars in our galaxies.

As is required in some of the relations we are presenting in this paper, we have estimated γ_* of our sample galaxies in both the V and 3.6-μm bands. We dedicate Appendices A and B to the description of the set of models and the methods used to derive these values.

6 SCALING RELATIONS

In this section, we show some of the classic scaling relations for the SAURON sample of early-type galaxies. Although much work has been devoted to these relations in the literature, mostly separating galaxies by their morphological classification, here we will focus on how deviations from scaling relations depend on the kinematic information and stellar populations from our integral-field data. Since we found no significant correlation with the level of kinematic substructure or environment in any of the considered scaling relations (demonstrated in Appendix C), we focus on differences between the SR E/S0, FR E/S0 and Sa galaxies.

In the following sections, we derive linear fits of the form $y = \alpha\, x + \beta$ to all relations, except the FP in Section 7. We started from the FITEXY[8] routine taken from the IDL Astro-Library (Landsman 1993) which fits a straight line to data with errors in both directions, which we extended to include possible correlations between the errors in both directions. To find the straight line that best fits a set of N data points x_j and y_j, with symmetric errors Δx_j and Δy_j and covariance Cov(x_j, y_j), the routine minimizes

$$\chi^2 = \sum_{j=1}^{N} \frac{(y_j - \alpha\, x_j - \beta)^2}{\Delta^2_{\mathrm{obs},\,j} + \Delta^2_{\mathrm{int}}}, \tag{5}$$

where the combined observational error is given by

$$\Delta^2_{\mathrm{obs},\,j} = (\Delta y_j)^2 + \alpha^2 (\Delta x_j)^2 - 2\,\alpha\, \mathrm{Cov}(x_j, y_j), \tag{6}$$

and Δ_{int} is the intrinsic scatter, which is increased until the value of χ^2 per degrees of freedom is unity. Next, finding the changes in α and β needed to increase χ^2 by unity yields the (1σ) uncertainties on the best-fitting parameters. The values of x_j are normalized by subtracting the corresponding observational quantities per galaxy by the median value of all galaxies. This choice for the reference value (or pivot point) minimizes the uncertainty in the fitted slope α and its correlation with the intercept β. The details and benefits of this approach are described in Tremaine et al. (2002).

In deriving the errors Δx_j and Δy_j, we include the uncertainties in all contributing quantities, that is, the errors in the distances, the photometric quantities, the kinematic quantities (stellar velocity dispersion) and the stellar population quantities. Correlations in the photometric quantities are taken into account via our Monte Carlo realizations of Section 4.1; for example, when deriving the error in $\langle\mu_\mathrm{e}\rangle = -2.5 \log \left[L_\mathrm{e}/(\pi R_\mathrm{e}^2)\right]$, we first compute from all realizations of L_e and R_e the corresponding $\langle\mu_\mathrm{e}\rangle$ values, and then derive the error as the (biweight) standard deviation. Similar Monte Carlo simulations of all quantities are used to calculate the covariance Cov(x_j, y_j), which can be significant especially when the same quantities are used in both x_j and y_j, such as R_e in the KR and the distance in the SLR.

Unless mentioned otherwise, for consistency and hence for easy comparison with most publications on scaling relations for early-type galaxies, only E/S0 galaxies with reliable distance estimates are included in the fits (i.e. 46 objects). The resulting best-fitting relations are shown in the figures themselves, while the best-fitting parameters and corresponding errors are given in Table 1. The values indicated by Δ_{fit} represent the scatter around the best-fitting relation in the vertical direction, that is, the (biweight) standard deviation of $y_j - \alpha\, x_j - \beta$, for the galaxies j used in the fit. The value in parentheses is the intrinsic scatter, calculated after subtracting in quadrature from Δ_{fit} the (biweight) mean of the combined observational

---

[8] Based on a similar routine by Press et al. (1992).

Table 1. Scaling relations' best-fitting parameters.

Relation (1)	Band (2)	α (3)	β (4)	γ (5)	δ (6)	$\Delta_{\rm fit}$ (7)	$\Delta_{\rm [SR]}$ (8)	$\Delta_{\rm [FR]}$ (9)	$\Delta_{\rm [Sa]}$ (10)	N (11)	Sample (12)
CMR	V	-0.06 ± 0.02	3.30 ± 0.02	–	–	0.092 ± 0.010	0.067 ± 0.009	0.101 ± 0.011	0.245 ± 0.010	46	E/S0
Colour–$\sigma_{\rm e}$	–	0.64 ± 0.07	3.27 ± 0.01	–	–	0.057 ± 0.011	0.019 ± 0.017	0.064 ± 0.010	0.295 ± 0.010	46	E/S0
KR	V	2.05 ± 0.22	19.75 ± 0.07	–	–	0.447 ± 0.061	0.400 ± 0.029	0.464 ± 0.072	0.743 ± 0.079	46	E/S0
SLR	V	-2.84 ± 0.22	-20.73 ± 0.07	–	–	0.464 ± 0.028	0.461 ± 0.026	0.489 ± 0.028	0.807 ± 0.040	46	E/S0
FJR	V	-4.99 ± 0.71	-20.61 ± 0.11	–	–	0.662 ± 0.071	0.672 ± 0.057	0.644 ± 0.088	0.811 ± 0.193	46	E/S0
FP	V	1.15 ± 0.05	0.34 ± 0.01	-8.81 ± 0.19	–	0.067 ± 0.015	0.044 ± 0.016	0.075 ± 0.017	0.161 ± 0.037	46	E/S0
FP	V	1.08 ± 0.04	0.33 ± 0.01	-8.56 ± 0.18	–	0.078 ± 0.018	0.051 ± 0.015	0.070 ± 0.018	0.149 ± 0.038	60	E/S0/Sa
FP + Hβ_0	V	1.30 ± 0.04	0.32 ± 0.01	-9.22 ± 0.19	0.77	0.073 ± 0.016	0.043 ± 0.014	0.077 ± 0.016	0.116 ± 0.038	60	E/S0/Sa
FP + γ_*	V	1.56 ± 0.13	0.32 ± 0.01	-9.03 ± 0.31	-0.55 ± 0.13	0.064 ± 0.031	0.021 ± 0.029	0.070 ± 0.029	0.088 ± 0.051	60	E/S0/Sa
CMR	[3.6]	-0.06 ± 0.01	3.29 ± 0.01	–	–	0.087 ± 0.010	0.060 ± 0.010	0.095 ± 0.011	0.234 ± 0.010	46	E/S0
KR	[3.6]	1.98 ± 0.27	15.94 ± 0.08	–	–	0.519 ± 0.082	0.464 ± 0.042	0.541 ± 0.085	0.745 ± 0.097	46	E/S0
SLR	[3.6]	-2.93 ± 0.26	-23.79 ± 0.08	–	–	0.541 ± 0.029	0.396 ± 0.024	0.553 ± 0.120	0.659 ± 0.128	46	E/S0
FJR	[3.6]	-5.62 ± 0.69	-23.69 ± 0.10	–	–	0.640 ± 0.069	0.669 ± 0.054	0.618 ± 0.085	0.911 ± 0.187	46	E/S0
FP	[3.6]	1.37 ± 0.05	0.33 ± 0.01	-8.06 ± 0.19	–	0.071 ± 0.014	0.037 ± 0.012	0.083 ± 0.017	0.224 ± 0.035	46	E/S0
FP	[3.6]	1.23 ± 0.04	0.32 ± 0.01	-7.49 ± 0.16	–	0.099 ± 0.016	0.053 ± 0.012	0.084 ± 0.017	0.191 ± 0.036	60	E/S0/Sa
FP + Hβ_0	[3.6]	1.47 ± 0.04	0.31 ± 0.01	-8.35 ± 0.18	0.96	0.082 ± 0.014	0.044 ± 0.011	0.080 ± 0.015	0.132 ± 0.036	60	E/S0/Sa
FP + γ_*	[3.6]	1.61 ± 0.12	0.32 ± 0.01	-8.39 ± 0.37	-0.60 ± 0.15	0.057 ± 0.041	0.012 ± 0.050	0.065 ± 0.036	0.096 ± 0.057	60	E/S0/Sa

Notes. Column (1): we use the following notations for each of the scaling relations:

CMR: $(V - [3.6])_{\rm e} = \alpha(M + 24) + \beta$ for the V band and $(V - [3.6])_{\rm e} = \alpha(M + 21) + \beta$ for the 3.6-µm band.

Colour–$\sigma_{\rm e}$: $(V - [3.6])_{\rm e} = \alpha \log(\sigma_{\rm e}/\sigma_{\rm ref}) + \beta$, with $\sigma_{\rm ref} = 150$.

KR: $\langle\mu_{\rm e}\rangle = \alpha \log(R_{\rm e}/R_{\rm ref}) + \beta$, with $R_{\rm ref}$ equal to 2.4 and 1.7 for the V and 3.6-µm bands, respectively.

SLR: $M = \alpha \log(R_{\rm e}/R_{\rm ref}) + \beta$, with $R_{\rm ref}$ equal to 2.4 and 1.7 for the V and 3.6-µm bands, respectively.

FJR: $M = \alpha \log(\sigma_{\rm e}/\sigma_{\rm ref}) + \beta$, with $\sigma_{\rm ref} = 150$.

FP: $\log(R_{\rm e}) = \alpha \log(\sigma_{\rm e}) + \beta\langle\mu_{\rm e}\rangle + \gamma$.

FP + Hβ_0: $\log(R_{\rm e}) = \alpha \log(\sigma_{\rm e}) + \beta\langle\mu_{\rm e}\rangle + \gamma + \delta \log({\rm H}\beta_0)$.

FP + γ_*: $\log(R_{\rm e}) = \alpha \log(\sigma_{\rm e}) + \beta\langle\mu_{\rm e}\rangle + \gamma + \delta \log(\gamma_*)$.

Note that the δ parameter for the FP + Hβ_0 term has been held fixed (see Section 7.4).

Column (2): photometric band of the fit.

Columns (3–6): best-fitting parameters and uncertainties.

Columns (7–10): intrinsic scatter and uncertainties for the fit and SR/FR/Sa families. Values for the CMR, colour–$\sigma_{\rm e}$ relation, SLR and FJR are expressed in mag, while the values for the KR are expressed in mag arcsec^{-2}. For the FP, the intrinsic scatter is given in dex along the $\log(R_{\rm e})$ direction.

Columns (11) and (12): number of objects in the fit and type of galaxies fitted. Only galaxies with good distance estimations have been included in the fit.

errors $\Delta_{\mathrm{obs,j}}$, which, as indicated in equation (6), include potential covariances between the variables.

The intrinsic scatter values and corresponding error estimates can be found in Table 1. We confirmed that well within these errors, the intrinsic scatter values are the same as Δ_{int} in equation (5) when the value of χ^2 per degrees of freedom is unity. The other quoted scatter values, $\Delta_{[...]}$, are based on *all* galaxies within the family/families indicated by the index in square brackets, that is, also the galaxies with distances based on their recession velocities.

6.1 Relations with colour

We presented a set of CMRs in different photometric bands in Papers XIII and XV. In both cases, the most deviant objects were galaxies displaying widespread ongoing star formation. Here, we bring a new element to these works by investigating the location of galaxies with distinct kinematic properties (e.g. SR/FR) in the CMR.

In Fig. 7 (top panels), we plot the CMRs for our sample galaxies using the effective colour $(V - [3.6])_{\mathrm{e}}$. There are two main sources that can change the slope and increase the intrinsic scatter in these CMRs: young stellar populations and dust extinction. They have opposite effects. Young populations will, in principle, shift galaxies down from the relation (galaxies become bluer), while dust will make galaxies appear redder than their stellar populations. Our sample contains galaxies which clearly exhibit dust (most notably Sa galaxies). Since we have made no attempt to correct for internal extinction, the position of these galaxies in this CMR cannot be used to infer information about their stellar populations. The reddest objects (NGC 1056, 2273, 4220, 4235 and 5953) in the plotted relations are indeed Sa galaxies with very prominent dust lanes.

The bottom left-hand panel of Fig. 7 shows the colour versus σ_{e} relation. Here both the FR and SR families define a much tighter sequence than in the CMRs shown in the top panels. Particularly striking are the relations defined by the SRs and FRs, with intrinsic scatters of only 0.019 and 0.064 mag, respectively, as opposed to the Sa galaxies with deviations of about 0.30 mag, similar to those of the CMRs. The Sa galaxies systematically populate a region above the best-fitting relation. Given the relative insensitivity of σ_{e} to dust (at least much less than absolute magnitudes in the optical), this diagram is potentially useful to remove dusty objects in samples destined for CMR studies. It also confirms that the average dust content is larger in spiral galaxies than in earlier-type systems. Despite these deviant objects, it is worth noting that there are a few Sa galaxies in the region populated by SR/FR galaxies.

As already shown in Papers XI, XIII and XV, our sample contains a number of objects with clear signs of widespread star formation (NGC 3032, 3156, 4150, 3489, 4369, 4383, 4405 and 5953). Following the arguments outlined above, one might expect these galaxies to display the bluest colours (in the absence of dust). Surprisingly, this is not the case. In order to understand this behaviour, we have plotted in the bottom right-hand panel of Fig. 7 the effective colour versus the $\mathrm{H}\beta_0$ index measured within the same aperture. In addition to our data points, we also include colour predictions from Marigo et al. (2008, hereinafter MAR08)[9] together with line-strength predictions from the recently released MILES models[10] (VAZ10). This combination of colours and line indices is consistent, in the sense that both predictions are based on the same set of isochrones (Girardi et al. 2000) and were computed for a Kroupa (2001) initial mass function (IMF). These isochrones take into account the latest stages of stellar evolution through the thermally pulsing asymptotic giant branch (TP-AGB) regime to the point of complete envelope ejection. These models show that the dependence of the $(V - [3.6])_{\mathrm{e}}$ colour on age is rather subtle even for young stellar populations, being much more sensitive to metallicity than age. This is the reason behind the lack of a strong signature of the youngest objects in the CMRs of Fig. 7.

Now that we have assessed that metallicity is the main driver of the $(V - [3.6])_{\mathrm{e}}$ colour, we can deduce from the colour–σ_{e} relation that there must be a strong correlation between metallicity and σ_{e}. We have made an attempt to determine this relation by computing the best linear relation between metallicity ([M/H]) and $V - [3.6]$ colour in the MAR08 models ($V - [3.6] = 0.73[\mathrm{M/H}] + 3.28$, see Appendix A), and then substituting that in the colour–σ_{e} relation found here. The selected galaxies are predominantly old and thus are well reproduced by SSP models. This yields a relation of the form

$$[\mathrm{M/H}] = 0.88\,(\pm 0.07)\log(\sigma_{\mathrm{e}}) - 1.92\,(\pm 0.16). \qquad (7)$$

A similarly strong correlation was presented in Paper XVII ($[\mathrm{Z/H}](R_{\mathrm{e}}) = 0.32\log(\sigma_{\mathrm{e}}) - 0.82$) from an independent set of model predictions (Schiavon 2007) and methodology (i.e. using line-strength indices rather than colours). Note, however, that the two relations cannot be directly compared as the one presented in Paper XVII is based on non-solar scaled stellar population models, while the one derived here is not. In order to compare them, we have determined the metallicity of our models using the relation from the MAR08 models and then adjusted it assuming $[\mathrm{Z/H}] = [\mathrm{M/H}] + 0.75[\alpha/\mathrm{Fe}]$, where the factor 0.75 is a constant that depends on the element partition used for the models (R. Schiavon, private communication) and $[\alpha/\mathrm{Fe}]$ is taken from Paper XVII. The slope of the resulting relation still appears to be a factor of 2 steeper than that of Paper XVII. The apparent inconsistency between the two determinations might indicate some issues in the modelling of the always-complex AGB phase. The comparison with other relations in the literature (e.g. Jørgensen 1999; Kuntschner 2000; Trager et al. 2000; Thomas et al. 2005; Sánchez-Blázquez et al. 2006a; Proctor et al. 2008; Allanson et al. 2009; Graves, Faber & Schiavon 2009) is not straightforward either, since, in addition to the stellar population models used, they are mostly based on central aperture measurements (both metallicity and velocity dispersion).

6.2 Kormendy and size–luminosity relations

The KR and SLR for the SAURON sample of galaxies are shown together in Fig. 8. As already noted by other authors, the value one obtains for these relations critically depends on the adopted selection criteria. In particular, the Malmquist bias caused by selecting galaxies according to their luminosities can have a large impact on the resulting best-fitting relation (Nigoche-Netro, Ruelas-Mayorga & Franco-Balderas 2008). The volume and luminosity range of our survey means we lack small, high surface brightness, faint objects (as estimated from a comparison with the parent sample of galaxies in the ATLAS$^{\mathrm{3D}}$ project, Cappellari et al. 2011). None the less, limiting our fit to galaxies with distances below 25 Mpc (where our sample does not suffer those limitations) results in best-fitting relations that are identical within the uncertainties. The comparison of our data in the KR and SLR with that of B03 shows that the strongest bias introduced in our analysis by the sample selection is

---

[9] http://stev.oapd.inaf.it/cmd, version 2.2

[10] http://miles.iac.es

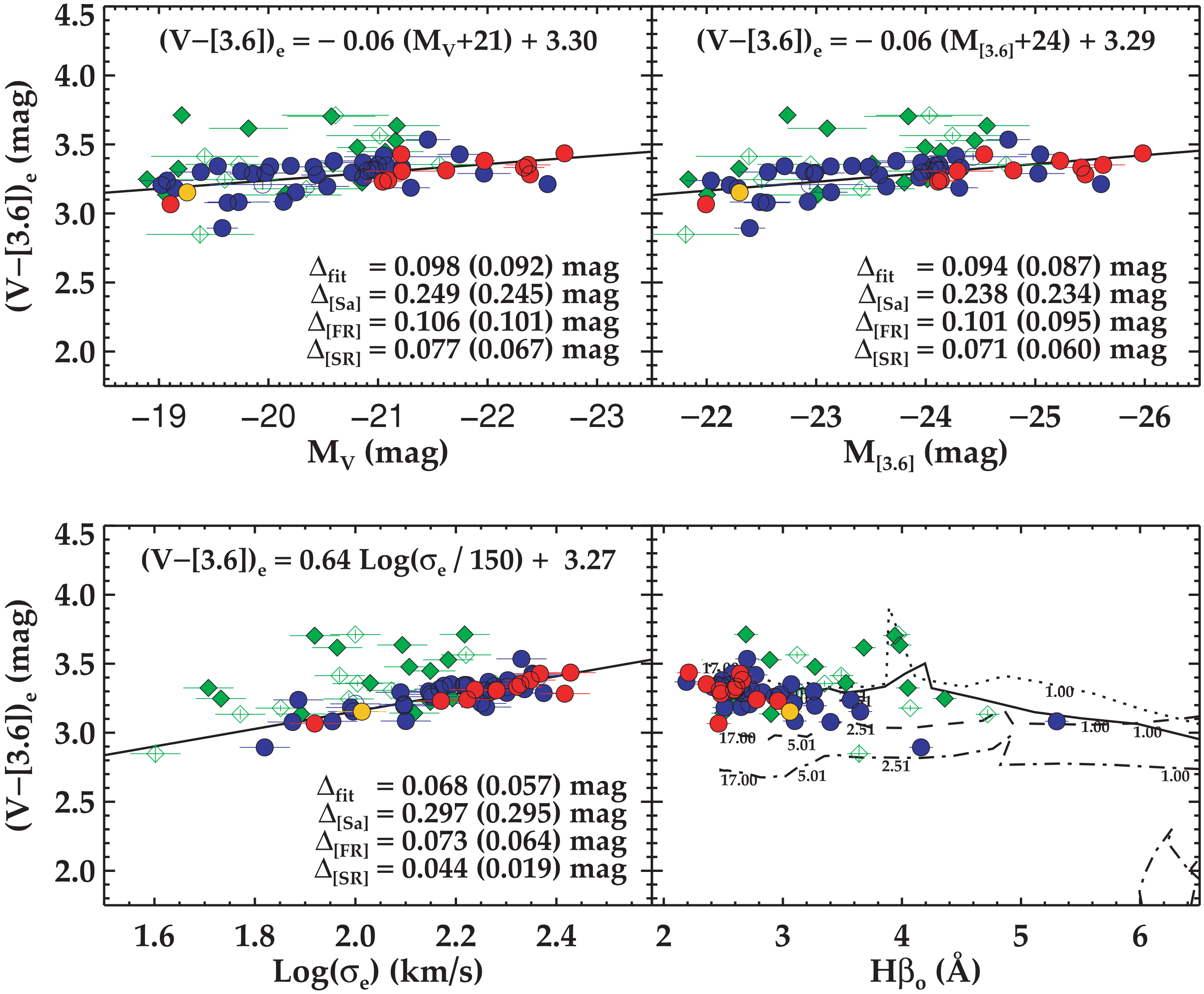

Figure 7. CMR, colour–σ_e relation and colour–Hβ_0 relation for the SAURON sample of galaxies. The best-fitting linear relations to the E/S0 galaxies with good distance determinations are indicated in each panel and are shown with the solid black lines. $\Delta_{\rm fit}$ indicates the observed and intrinsic scatters (the latter in parentheses) for the galaxies used to obtain the fit, while $\Delta_{[...]}$ represent the measured values for the different families around the best-fitting relations. Colours and symbols are as in Fig. 3. The lines in the bottom right-hand panel correspond to the MAR08 model colour predictions combined with MILES (VAZ10) Lick/IDS line-strength indices for different metallicities (see Section 6.1 for details): [M/H] = [−0.71 (dot–dashed), −0.40 (dashed), 0.00 (solid), +0.20 (dotted)]. For reference, some ages (in Gyr) are indicated along the different metallicity tracks. Peaks seen in the colour tracks are due to an enhancement in the production rate of AGB stars that causes a transient red phase in the integrated SSP colours (see Girardi & Bertelli 1998).

in mean surface brightness. With the exception of NGC 5845 (the galaxy with the smallest R_e), our galaxies seem to populate rather homogeneously the area defined by the B03 sample for $\langle\mu_{e,V}\rangle \lesssim$ 21 mag arcsec^{-2}. This implies a shallower KR and a steeper SLR than in the more complete B03 sample.

The observed scatter around the best-fitting relations is consistent with that found in other studies for galaxies within the same magnitude range (e.g. Nigoche-Netro et al. 2008). It appears that there is still a significant amount of intrinsic scatter in both relations, with the SR family displaying the smallest values. SR galaxies tend to populate the high-luminosity end (with the exception of NGC 4458), while FR galaxies extend across the whole luminosity range displayed by our sample. In general, Sa galaxies appear to be fainter (by ≈0.8 mag) than SR/FR galaxies of the same size. This result is consistent with the observed strong dependence of these relations on morphological type (e.g. Courteau et al. 2007).

One interesting feature is the lack of large, high surface brightness (or small and very luminous) galaxies. This *zone of avoidance* was already noted by Bender et al. (1992) and has been later better defined by D'Onofrio et al. (2006) and Cappellari et al. (2011).

6.3 Faber–Jackson relation

In Fig. 9, we show FJRs for our sample. As in previous relations, the SR family tends to occupy the high-luminosity end of the relations. Sa galaxies, however, deviate from the best-fitting relations in the sense that they systematically populate high luminosities for a given σ_e (for $\sigma_e \lesssim 125$ km s^{-1}). Disc galaxies are often characterized by

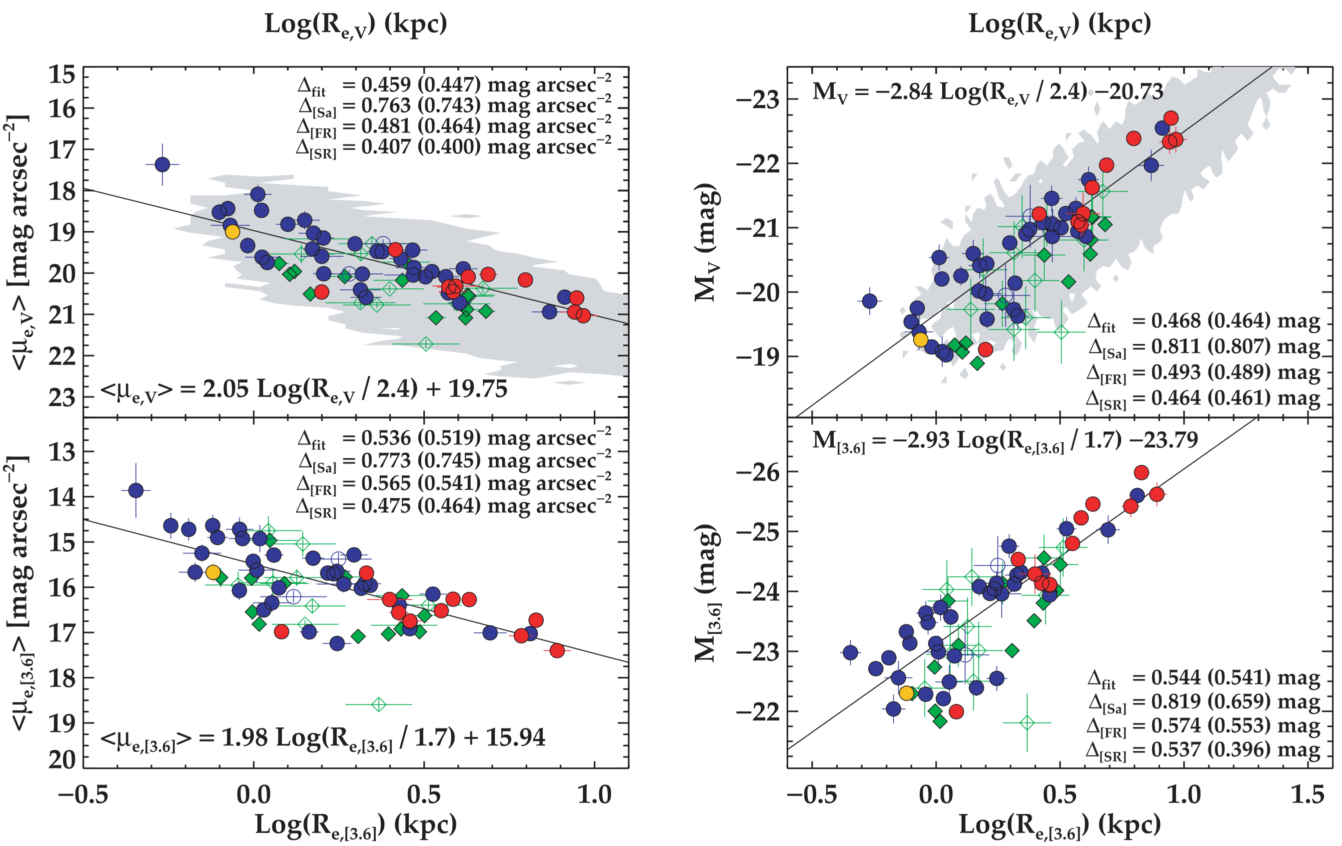

Figure 8. KR and SLR for the galaxies in the SAURON sample in the *V* and 3.6-μm bands. Symbols are as in Fig. 3. The thick solid line is the best-fitting relation (as indicated in the equation in each panel). $\Delta_{\rm fit}$ indicates the observed and intrinsic scatters (the latter in parentheses) for the galaxies used to obtain the fit, while $\Delta_{[...]}$ represent the measured values for the different families around the best-fitting relations. The grey area marks the extent of the B03 sample.

the Tully–Fisher relation (Tully & Fisher 1977) instead of the FJR. This is because in low-mass systems the maximum rotational velocity is a much better tracer of total mass than the traditionally measured central velocity dispersions. The use of a large aperture for the velocity dispersion measurement ($\sigma_{\rm e}$) presented here significantly helps to improve matters by using a parameter close to the integrated second moment (see Paper IV). We believe that the observed offset is mainly a stellar population effect, whereby Sa galaxies are on average younger (and thus have in general lower stellar mass-to-light ratios) than earlier types, as already discussed in the literature (e.g. Paper XI). This effect is further supported by the best-fitting relation for the SRs (e.g. predominantly old systems). As shown in the figure, the slope of the relation for the SRs is larger (dashed line) than the original fit and is in better agreement with B03. Nevertheless, the number of SRs in our sample is rather limited and thus complete samples (e.g. from the ATLAS$^{\rm 3D}$ project) are required to confirm the observed trend.

The FJR for our sample appears to ‘bend’ towards low-$\sigma_{\rm e}$ values at low luminosities. There is a hint of this feature in the relations for the Coma Cluster by Bower et al. (1992) and Jørgensen et al. (1996), but it is somehow not seen in other relations in the literature based on much larger numbers of galaxies (e.g. B03; La Barbera et al. 2010). This might be because galaxies with low velocity dispersions are often removed from the samples. Irrespective of selection effects, the slopes derived here are slightly shallower than previously found (e.g. Pahre 1999). In part this is because it is common to use central velocity dispersions, which will increasingly deviate from the values reported here (measured in a larger aperture) for larger galaxies, as the velocity dispersion gradients are steeper in the inner parts of larger galaxies.

7 FUNDAMENTAL PLANE

In this paper, we adopt the following notation for the FP:

$$\log(R_{\rm e}) = \alpha \log(\sigma_{\rm e}) + \beta \langle \mu_{\rm e} \rangle + \gamma. \qquad (8)$$

The multivariate nature of the FP makes common least-squares minimization algorithms not suitable to determine the main parameters (α, β, γ). The literature is vast on alternative methods (e.g. Graham & Colless 1997; La Barbera, Busarello & Capaccioli 2000; Saglia et al. 2001), several of which we tested to yield consistent best-fitting parameters within the corresponding estimated errors. The FP results presented in this paper are determined via an orthogonal fit by minimizing the sum of the absolute residuals perpendicular to the plane (e.g. Jørgensen et al. 1996). As in Section 6, we include the uncertainties in all contributing quantities and take into account correlations in the photometric quantities via our Monte Carlo realizations.

In addition to the fitting scheme, sample selection biases in any of the quantities of equation (8) can have an important impact on the resulting coefficients (Nigoche-Netro, Ruelas-Mayorga & Franco-Balderas 2009). We have tested the sensitivity of our best-fitting parameters to magnitude and distance (the two main selection criteria in our sample). Our sample is a good representation, in terms of luminosity, of the complete early-type galaxy population up to a distance of 25 Mpc, beyond which we lack small, faint, high

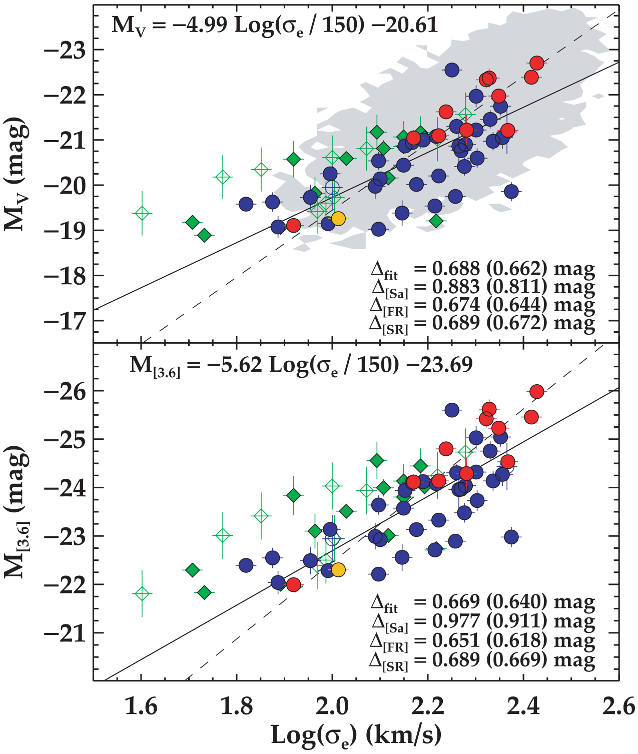

Figure 9. FJR for the galaxies in the SAURON sample in the V and 3.6-μm bands. Symbols are as in Fig. 3. The solid line is the best-fitting relation (as indicated in the equation at the top left-hand side in each panel). The dashed line shows the best fit to the SR family (e.g. predominantly old systems). $\Delta_{\rm fit}$ indicates the observed and intrinsic scatters (the latter in parentheses) for the galaxies used to obtain the fit, while $\Delta_{[...]}$ represent the measured values for the different families around the best-fitting relations. The grey area marks the extent of the B03 sample.

surface brightness objects. Nevertheless, the inclusion of galaxies at larger distances hardly alters the best-fitting parameters. In terms of luminosity alone, the best-fitting parameters remain within the uncertainties as long as the faintest level in absolute magnitude is brighter than $M_V \approx -19$ and $M_{[3.6]} \approx -22$ mag. Therefore, while distance has no major impact on the best-fitting parameters, the removal of the fainter objects in our sample does. As shown in fig. 7 of Hyde & Bernardi (2009), the expected bias in the α parameter due to our sample selection in terms of absolute magnitude is below 10 per cent. As in other relations, we restrict our fit to E/S0 galaxies with good distance determinations (i.e. filled SR/FR galaxies in the relations). From the comparison of our data with those of B03, we have established that the lack of objects with $\langle\mu_{{\rm e},V}\rangle \lesssim 21.0$ mag arcsec^{-2} in our sample effectively means that we miss galaxies with $R_{\rm e} \gtrsim 12$ kpc. We have checked, using the B03 sample, that this effect does not seem to bias our results in any particular way.

7.1 Classic FP

In Fig. 10, we present the FP for our sample galaxies in both the V band and the 3.6-μm band. Sa galaxies share the same relation as defined for early-type systems and are not clearly displaced below the relation as they usually are. We believe that the main reason for this behaviour is the way we have derived the quantities involved. When including spiral galaxies in the FP, it is customary to measure the photometric and spectroscopic quantities only within the bulge-dominated region (e.g. Falcón-Barroso et al. 2002). Here we have measured the half-light radius, mean surface brightness and velocity dispersion in a consistent and homogeneous way for all galaxies, regardless of morphological type. The importance of also computing the velocity dispersion within the same half-light radius was already shown in Fig. 4: even though the photometric quantities taken from different literature sources for galaxies in our sample individually might vary substantially, when combined with a consistently measured integrated velocity dispersion, they all fall on our best-fitting classic FP. In Section 7.5, we investigate the effects on the best-fitting parameters if non-consistent velocity dispersion measurements are used.

The best-fitting coefficients in both bands are somewhat inconsistent with some of the most recent works in the literature (e.g. Pahre 1999; Bernardi et al. 2003b; Proctor et al. 2008; Hyde & Bernardi 2009; La Barbera et al. 2010). Although difficult to assess accurately, we believe that the main differences are due to a combination of photometric bands employed, fitting methods and, especially, sample selection (since we include the Sa galaxies, unlike previous works). There is nevertheless a large disparity in the literature regarding the value of the FP coefficients. There seems to be, however, a consensus on the fact that α changes gradually with photometric band (increasing with wavelength) while β remains almost constant (e.g. Hyde & Bernardi 2009). The relations derived here share that property. The parameters also deviate from the virial theorem predictions (i.e. $\alpha = 2$ and $\beta = 0.4$ in the notation used here), an effect known as the '*tilt*' of the FP. At first sight, it might seem surprising that the β coefficient in the V band, more sensitive to young stellar populations than infrared bands, has a similar value to that in the 3.6-μm band. It is important to remember, however, that the γ parameter, while assumed constant, is in fact a function of the total mass-to-light ratio (M/L), which is not necessarily constant among galaxies. In fact, this M/L depends on the stellar populations, that is, one can express the total M/L as a function of the stellar mass-to-light ratio γ_* and the relative fraction of luminous to dark matter. It seems that during the fitting process stellar population effects conspire to keep β constant while affecting α and γ.

7.2 Outliers and residuals

Not all the galaxies in our sample appear to follow the main FP relation. NGC 4382 is a well-known shell galaxy (e.g. Kormendy et al. 2009) which must have suffered some recent interaction event. It contains a rather young nucleus (3.7 Gyr, see Paper XVII), it is the youngest of all the non-CO detected SAURON galaxies (Combes, Young & Bureau 2007) and it also displays a prominent central velocity dispersion dip (see Paper III). NGC 1056, 4369, 4383, 5953 and 7742 are Sa galaxies that contain a significant fraction of young stars within $R_{\rm e}$ (see Paper XI). NGC 3489 is one of the few early-type galaxies with a strong starburst in the last 2 Gyr (see Paper XVII). NGC 7332 was already recognized as an outlier of the FP in the optical and near-infrared bands by Falcón-Barroso et al. (2002). Although it shows signs of widespread young populations, it is not at the level of other early-type galaxies. Nevertheless, this object is peculiar in that it is rich in kinematic substructure (Falcón-Barroso et al. 2004) and might have suffered from a recent interaction with NGC 7339. Moreover, the presence of two gaseous counter-rotating discs (Plana & Boulesteix 1996) suggests that this galaxy might not be in dynamical equilibrium. It is interesting to note that the object in our sample with the strongest presence of widespread young populations, NGC 3032, does not deviate at all from the best fits.

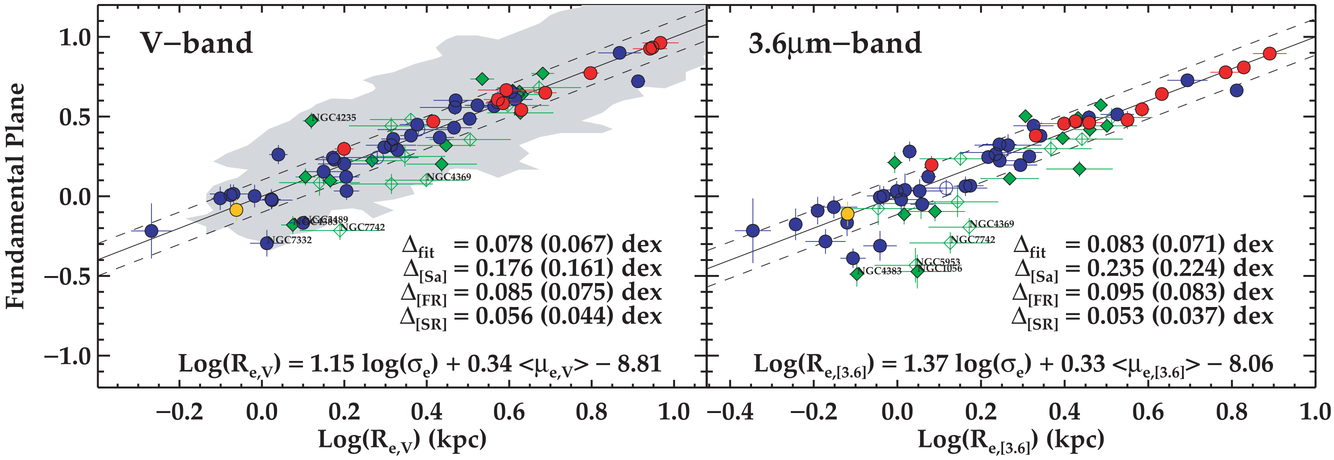

Figure 10. Edge-on views of the FP relation for the galaxies in the SAURON sample of galaxies in the *V* and 3.6-μm bands. Symbols are as in Fig. 3. The dashed lines mark the 1σ uncertainty [measured in $\log(R_e)$] considering all objects. The solid line is the best-fitting relation (as indicated in the equation in each panel). $\Delta_{\rm fit}$ indicates the observed and intrinsic scatters (the latter in parentheses) measured along the $\log(R_e)$ axis for the galaxies used to obtain the fit, while $\Delta_{[...]}$ represent the measured values for the different families around the best-fitting relations. The grey area marks the extent of the B03 sample.

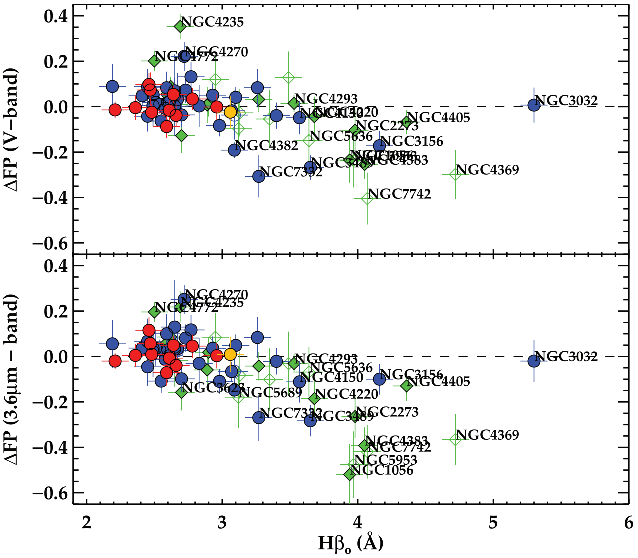

Figure 11. Residuals [along the $\log(R_e)$ axis] of the FPs in Fig. 10 as a function of the Hβ_0 line-strength index. Symbols are as in Fig. 3.

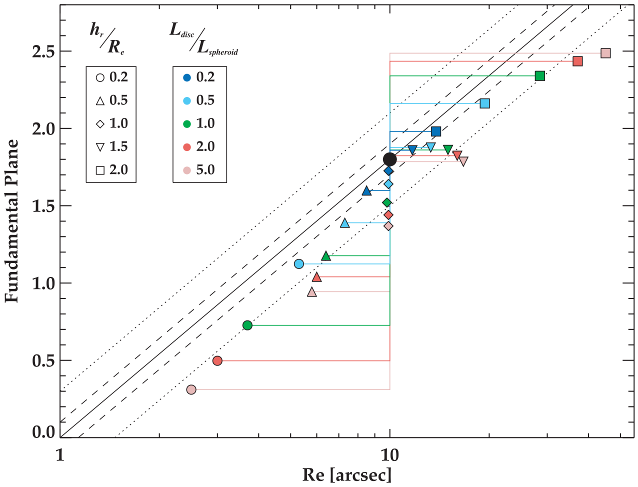

Figure 12. Simple experiment to show the effects of adding a disc to a spheroid at the location of galaxies in the FP (see Section 7.3). The black dot marks the location of a pure spheroid, by construction on the FP. The black solid line marks the FP and, for reference, the dashed and dotted lines denote the 1 and 3σ scatter in the relation shown in Fig. 10. Different symbols indicate the ratio between the scalelength of the added disc (h_r) and the effective radius (R_e) of the underlying spheroid. Colours correspond to different fractions of disc light ($L_{\rm disc}$) relative to the spheroid ($L_{\rm spheroid}$).

Individual inspection of the outliers to understand the reasons for their unusual location with respect to the main FP strongly suggests young stellar populations as a common factor. We investigate this further by exploring whether the residuals correlate with stellar population quantities, such as Hβ_0, shown in Fig. 11. A correlation with the Hβ_0 index indeed exists in both bands. With the exception of NGC 3032 noted above, galaxies with young stellar populations are systematically located below the main relation. These residuals suggest that, while metallicity gradients may contribute to the scatter in the FP, young populations are the dominant factor.

7.3 Influence of discs

In order to disentangle the possible effects on the FP due to structural non-homology in galaxies from those due to young stellar populations, we have carried out a simple experiment illustrated in Fig. 12. We have defined a mock early-type galaxy as a spheroid with a light profile described by a de Vaucouleurs' law. By construction, we put this spheroid on a generic FP (black filled circle and solid line). In order to assess the impact of an additional disc component, we added exponential discs to the spheroid, with the scalelengths of 0.2, 0.5, 1.0, 1.5 and 2.0 times the R_e of the spheroid (circles, upward triangles, diamonds, downward triangles and squares, respectively). For reference, we note that the typical values are $\gtrsim$5 for late-type galaxies (Balcells, Graham & Peletier 2007). Additionally, we set the light of the disc to be 0.2, 0.5, 1.0, 2.0 and 5.0 times the light of the spheroid (dark blue, cyan, green, red, and pink, respectively). We have analysed the growth curves of all these mock galaxies in the same way as the real galaxies presented in this paper. We have assumed the same σ_e for all mock galaxies as its value does not seem to depend on the Sérsic n used in the growth curves of our real galaxies.

The figure shows that with an increase in the disc light fraction, the mock galaxies tend to deviate more and more from the original FP. This is expected as the increase in light will lead to higher surface brightnesses, which in turn will push the objects below the relation. It is interesting, however, that the deviations only seem significant when the light fraction of the disc relative to the bulge is above a factor of 2, regardless of the size of the disc relative to the spheroid. We note the large excursions in R_e and vertical directions for large disc light fractions. Fig. 12 also shows the effect of a compact or extended disc relative to the underlying spheroid. Compact bright discs tend to shift the galaxies towards the left-hand side of the relation, while extended ones shift towards the right-hand side. It is important to realize that the presence of a disc has little influence on the end location of a galaxy, unless the disc is rather bright relative to the spheroid.

There are, in principle, other sources for the scatter and tilt of the FP that we are not accounting for here in detail: projection effects, rotation, structural homology, etc. All those, besides stellar populations, have been studied in detail in the literature (e.g. Guzman, Lucey & Bower 1993; Saglia et al. 1993; Prugniel & Simien 1994; Ciotti, Lanzoni & Renzini 1996; Jørgensen et al. 1996; Graham & Colless 1997; Prugniel & Simien 1997; Pahre et al. 1998; Mobasher et al. 1999; Trujillo, Burkert & Bell 2004), although with different and sometimes conflicting conclusions. Recent studies, however, point to stellar populations and dark matter as the main drivers (Treu et al. 2006; Paper IV; Bolton et al. 2008; Graves & Faber 2010). In this paper, we focus on the effect of stellar populations only.

Results on the importance of young stellar populations in determining the location of galaxies in the FP were already highlighted in Paper XIII, based on *GALEX* observations in the ultraviolet regime. Although the analysis in that paper was limited to fewer galaxies than the sample presented here, it appears that an important fraction of the tilt and scatter of the ultraviolet FPs is due to the presence of young stars in preferentially low-mass early-type galaxies. Triggered by those results, we have attempted here to take a step further and correct the FP for stellar population effects in order to bring *all* galaxies into a common FP relation. The results of this exercise are discussed in the following section.

7.4 FP corrected for stellar populations

A first test to assess the effect of young stellar populations on the tilt of the FP is to derive the best-fitting relation after restricting the sample to predominantly old galaxies, that is, SRs and FRs with $\mathrm{H}\beta_0 \leq 3.0$ Å, and good distance determinations (35 objects). This simple experiment yields the best-fitting parameters $\alpha = 1.39$, $\beta = 0.35$ and $\gamma = -9.61$ in the V band and $\alpha = 1.63$, $\beta = 0.34$ and $\gamma = -8.85$ in the 3.6-μm band. The dramatic change compared to Fig. 10 is the sudden increase in the α parameter, while β remains almost unaltered. This object selection reduces the tilt of the FP and brings it much closer to the virial prediction. Nevertheless, it is worth noting that the two α values (i.e. one for each band) are not close to each other, as one might expect if we had fully corrected for stellar population effects and hence were left with effects, in particular the luminous-to-dark matter fraction, that are insensitive to wavelength.

Considering the residuals in Fig. 11, one can take this experiment a step further and try to fully compensate for stellar populations (young and old) simultaneously. $\mathrm{H}\beta_0$ is not a quantity that directly enters the FP equation as defined in equation (8). However, as stated in Section 7.1, the γ coefficient does depend on stellar populations via γ_*. We have made an attempt to estimate the effective γ_* for each galaxy based on the combined MILES+MAR08 models, assuming a combination of two SSPs as the baseline SFH (see Appendices A and B). The relations between our computed γ_* and observed $\mathrm{H}\beta_0$ index are shown in Fig. 13, one for each photometric band. It appears that $\mathrm{H}\beta_0$ is strongly correlated with our measured γ_* and thus could be used as a rough surrogate for γ_*. This behaviour was already given in Paper IV for the $\mathrm{H}\beta$ index. The fitted relations, despite being strong, have two important shortcomings: (1) they overpredict γ_* at the low-$\mathrm{H}\beta_0$ end; and (2) they are rather uncertain for $\mathrm{H}\beta_0$ values above 3.0 Å. The first effect is an inherent limitation of the models used, that is, any given set of models predict a maximum γ_* for a given IMF. The second effect is related to the wide range of allowed γ_* for a given $\mathrm{H}\beta_0$ value, as parametrized by the set of two SSP models used here.

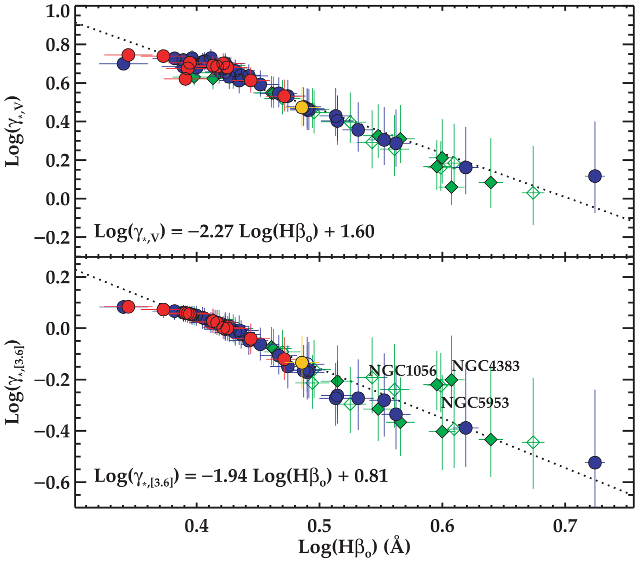

Figure 13. γ_* versus $\mathrm{H}\beta_0$ relations for the SAURON sample galaxies in the V and 3.6-μm bands. Best-fitted (log–log) linear relations are indicated in each panel and plotted with a dotted line. γ_* values have been determined as explained in Appendix B.

There are a few notable exceptions to the strong correlation at 3.6 μm. These are objects located very close to the peaks of the $V - [3.6]$ colour in the MAR08 models for solar metallicities or above (i.e. NGC 1056, 4383 and 5953; see Fig. 7). Their $\mathrm{H}\beta_0$ values range from 3.8 to 4.2 Å. Since our $\gamma_{*,[3.6]}$ predictions are made after correcting for the colour difference with $\gamma_{*,V}$ (see Appendix A), it is not completely surprising that the $\gamma_{*,[3.6]}$ values in that region somehow deviate from the trend defined by neighbouring objects. However, sudden jumps in γ_* of that magnitude seem unrealistic for these galaxies, and thus we opted to correct their values using the linear γ_* versus $\mathrm{H}\beta_0$ relation in that band presented in Fig. 13.

Considering the nearly linear log–log relations between γ_* and $\mathrm{H}\beta_0$, we can re-write the original FP equation in terms of these variables:

$$\log(R_e) = \alpha' \log(\sigma_e) + \beta' \langle \mu_e \rangle + \gamma' + \delta' \log(\mathrm{H}\beta_0), \tag{9}$$

$$\log(R_e) = \alpha' \log(\sigma_e) + \beta' \langle \mu_e \rangle + \gamma' + \delta' \log(\gamma_*), \tag{10}$$

where γ' now depends (mainly) on the luminous-to-dark matter ratio.

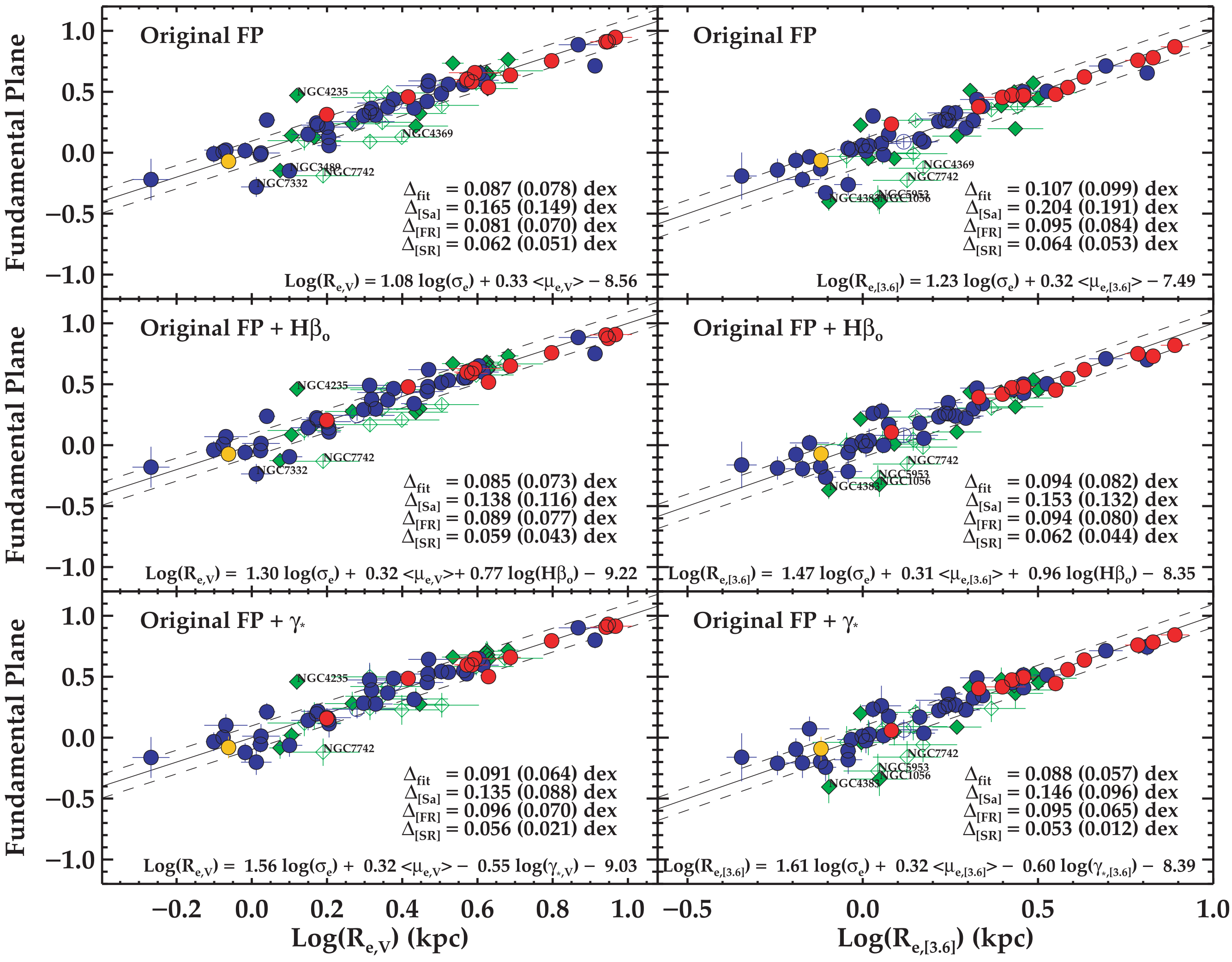

Figure 14. Edge-on views of the FP relations for the galaxies in the SAURON sample in the V and 3.6-μm bands. Symbols are as in Fig. 3. Top row: original FP relation. Middle row: original FP relation with an Hβ_0 term. Bottom row: original FP relation with a γ_* term. The dashed lines mark the 1σ uncertainty [measured along the log (R_e) axis] considering all objects. The solid line is the best-fitting relation (as indicated in the equation in each panel). Δ_fit indicates the observed and intrinsic scatters (the latter in parentheses) measured along the log (R_e) axis for the galaxies used to obtain the fit, while $\Delta_{[...]}$ represent the measured values for the different families around the best-fitting relations.

In Fig. 14, we plot the results of this experiment. In order to make a meaningful estimate of the effects of the stellar populations, we consider *all* objects with good distance estimates in the fit (60 galaxies, as opposed to the fits in Fig. 10 where only 46 E and S0 galaxies with good distances were considered). We perform this test in both bands. The top row in Fig. 14 shows the resulting fits using the classic FP definition (equation 8), whereas the middle and bottom panels present the fits including the Hβ_0 and γ_* terms (equations 9 and 10). It seems that the inclusion of the Sa galaxies in the fits of the original FP relation (top panels) results in smaller slopes, which translates into larger departures from the virial expectations.

Our first attempt to bring deviant objects closer to the relation is to add the Hβ_0 term in the FP relation. Unfortunately, leaving all the input parameters unconstrained results in very poor fits that, while successful in bringing back the most deviant galaxies, display much larger scatters than previous relations derived in this paper and, more importantly, have unreasonable coefficients. In order to get meaningful fits, we have instead fixed the Hβ_0 terms to the coefficients expected from the fits to the original FP residuals versus Hβ_0 shown in Fig. 11. The results of fixing this term are shown in the middle panels. These fits are able to bring the young objects much closer to the relations and at the same time to slightly reduce the intrinsic scatters. The α' coefficients have increased with respect to the original relation, getting them a step closer to the virial prediction, while the β' values have only changed within the uncertainties ($\approx$0.01). The main disadvantage of Hβ_0 as a substitute to γ_* can be seen in the case of NGC 3032. As already shown in Fig. 13, this galaxy is a deviant object in the γ_* versus Hβ_0 relation, and this translates in it being pushed out of the relation (its measured Hβ_0 value overpredicts its true γ_*).

Finally, in the bottom panels of Fig. 14, we add the γ_* term in the FP relation. In this case, the unconstrained fits result in physically meaningful coefficients, while at the same time bringing the most deviant points closer to the relation. The best-fitting parameters reduce the FP tilt compared to the original relations by almost 50 per cent in each band. It is important to remark that best-fitting coefficients in both bands are now consistent within the errors, as expected if we had corrected for the effects of stellar populations.

The coefficients, at least in the 3.6-μm band, are also within the uncertainties of those obtained by fitting the old galaxies only (see above). While in the *V* band most of our young objects get closer to the relation, in the 3.6-μm band, this is not the case (even though we have corrected their γ_* estimates based on Fig. 13 as explained above). In fact, these objects cannot be brought back to the 3.6-μm band relation even with the most extreme γ_* values allowed by our stellar population fitting procedure.

As an additional exercise (not shown here), we have studied the effect of using the $(V - [3.6])_{\rm e}$ colour, instead of $\mathrm{H}\beta_0$ or γ_*, in reducing the tilt of the FP. As expected, given the poor sensitivity of this colour to age (as shown in Fig. 7), this quantity does not help reducing the tilt. At the same time, it also demonstrates that metallicity cannot be a major player in producing the tilt (since this colour correlates strongly with metallicity, see Appendix A).

It is important to remind the reader that we have only corrected for the effects produced by stellar populations and partly by rotation (by using $\sigma_{\rm e}$). Still there are a number of other factors that influence the final location of galaxies in the FP. The complex manner in which star formation and dust compensate each other might be at the heart of the location discrepancies of some of the objects in the *V*- and 3.6-μm-band FPs. Nevertheless, the results of our exercise demonstrate that it is possible to correct for stellar population effects and bring most galaxies to a common relation, regardless of their morphological type and photometric band employed by including sensible estimates of the stellar mass-to-light ratios. This approach was previously adopted by Prugniel & Simien (1996) in a sample of elliptical galaxies and has been more recently exploited by other groups on much larger samples, though still restricting the analysis to early-type systems (e.g. Allanson et al. 2009; Hyde & Bernardi 2009; Graves & Faber 2010). Our results are largely consistent with those.

7.5 Scatter in the FP

One of the most striking features observed in our fits of the FP is the very tight relation defined by the SR galaxies in both bands. This is not a totally unexpected result as SR galaxies are uniformly old, but it is remarkable how the trend is kept even for smaller and fainter galaxies (as SR galaxies extend over the whole range in luminosity of our sample). The FR family displays slightly larger rms ($\Delta_{\rm [FR]}$) values. The scatter of the Sa galaxies appears to be the largest of the cases we have studied here. The different panels in Figs 10 and 14 show the observed as well as the intrinsic scatter (within brackets) for each family. For easy comparison with other works in the literature, we choose to provide them measured along the $\log(R_{\rm e})$ direction.

The first thing to note for the classic fits in Figs 10 and 14 is the differences between the values reported. The scatter for the Sa galaxies in the first figure is larger than in the second. Conversely, the rms for the SR/FR families is smaller in the first figure than in the second one. This is simply due to the fact that for determining the FP we fit only the SR/FR galaxies in Fig. 10, while Fig. 14 includes the Sa galaxies as well. If we focus on the latter figure, we observe, apart from a change in the slopes, an improvement (i.e. a decrease) in the scatter for *all* families when we include the $\mathrm{H}\beta_0$ and γ_* terms to correct for the effects of young populations. It is also interesting to note that once corrected for this effect, the intrinsic values found for the different families indicate that while FR and Sa galaxies are consistent within the uncertainties, they are clearly different from those of the SRs. This finding emphasizes the results presented in Paper IX and subsequent papers in the SAURON series suggesting, based on our kinematic classification, that these may be intrinsically a different kind of galaxies. This clear distinction is not found between morphologically classified elliptical and lenticular galaxies.

The comparison of the scatter presented here with others in the literature has to be treated with caution as, while most works concentrate in E/S0 galaxies, the different samples were selected with very different criteria in terms of luminosity or velocity dispersion. In addition, the methods used to fit the relation can affect this comparison, although the minimization of the residuals via an orthogonal fit is the most widely adopted. There is a general agreement that the observed scatter is consistent among photometric bands, a result we share. The typical observed scatter for a general population of E/S0 galaxies is around 0.10 dex in $\log(R_{\rm e})$ (e.g. Jørgensen et al. 1996; Pahre et al. 1998; Zibetti et al. 2002; La Barbera et al. 2010), with decreasing values (∼0.07 dex) as soon as low velocity dispersion ($\sigma \lesssim 70\ \mathrm{km\,s^{-1}}$) or fainter galaxies ($M_r \gtrsim -23$ mag) are removed from their samples (e.g. Jørgensen et al. 1996; Bernardi et al. 2003b; La Barbera et al. 2008; Gargiulo et al. 2009). The values measured here for the SR/FR are in good agreement with those in the literature for general samples of E/S0 galaxies. In the specific case of Jørgensen et al. (1996), the lowest observed scatter, 0.047 dex, is measured for galaxies with no presence of discs and $M_r \lesssim -23.1$ mag. They report that this value is consistent with the measurement errors. The closest set of galaxies in our sample matching those constraints is the SR family. For this group, we find a very small amount of intrinsic scatter left, 0.021 ± 0.029 and 0.012 ± 0.050 dex in the *V* band and 3.6-μm band, respectively. The uncertainties in our estimates suggest that the scatter around the best-fitting FP is fully explained by the observational errors.

Another interesting point to discuss is whether the use of a large-aperture velocity dispersion, instead of a central value, helps to reduce the intrinsic scatter in the relation. This was nicely discussed in Graham & Colless (1997) and Busarello et al. (1997), using samples of elliptical and lenticular galaxies and dynamical models with some assumptions on the shape of the velocity ellipsoid. The SAURON spectrograph gives us now the chance to repeat this exercise using real data. We have measured the velocity dispersion within $R_{{\rm e},V}/8$ ($\sigma_{{\rm e},8}$) for our sample of galaxies and then fitted the FP in the same manner as done in Fig. 14. This is presented in Fig. 15. The different panels show that the use of a small-aperture velocity dispersion affects the resulting fits in two important ways: (1) increasing the intrinsic scatter of the relations for all families of objects; and (2) the measured parameter α has lower values than those obtained when $\sigma_{\rm e}$ is used. The first point is mainly due to the fact that with the smaller aperture we are probing regions of the galaxies where intense star formation is taking place or inner discs exist, and thus the measured velocity dispersion is more representative of areas around the nuclei than the galaxy as a whole. The second effect is likely produced by the fact that $\sigma_{{\rm e},8}$ systematically departs from $\sigma_{\rm e}$ (i.e. it is larger) for increasing $\sigma_{\rm e}$ values. This, together with the expected relation between $R_{\rm e}$ and $\sigma_{\rm e}$ (given the SLR and FJR), helps to reduce the measured slope of the FP relation. Overall, we estimate an increase of around 15 per cent in the intrinsic scatter and an average 10 per cent decrease in α as a result of using a central value for the velocity dispersion term. It is also worth noting that the scatter of the Sa galaxies has not increased as much as for the SR and FR families. This supports the idea that the star formation in early-type systems takes place predominantly in their central regions, while for Sa galaxies this can happen over a much larger region (see also Paper XI), and therefore it does not necessarily make much difference to measure the velocity

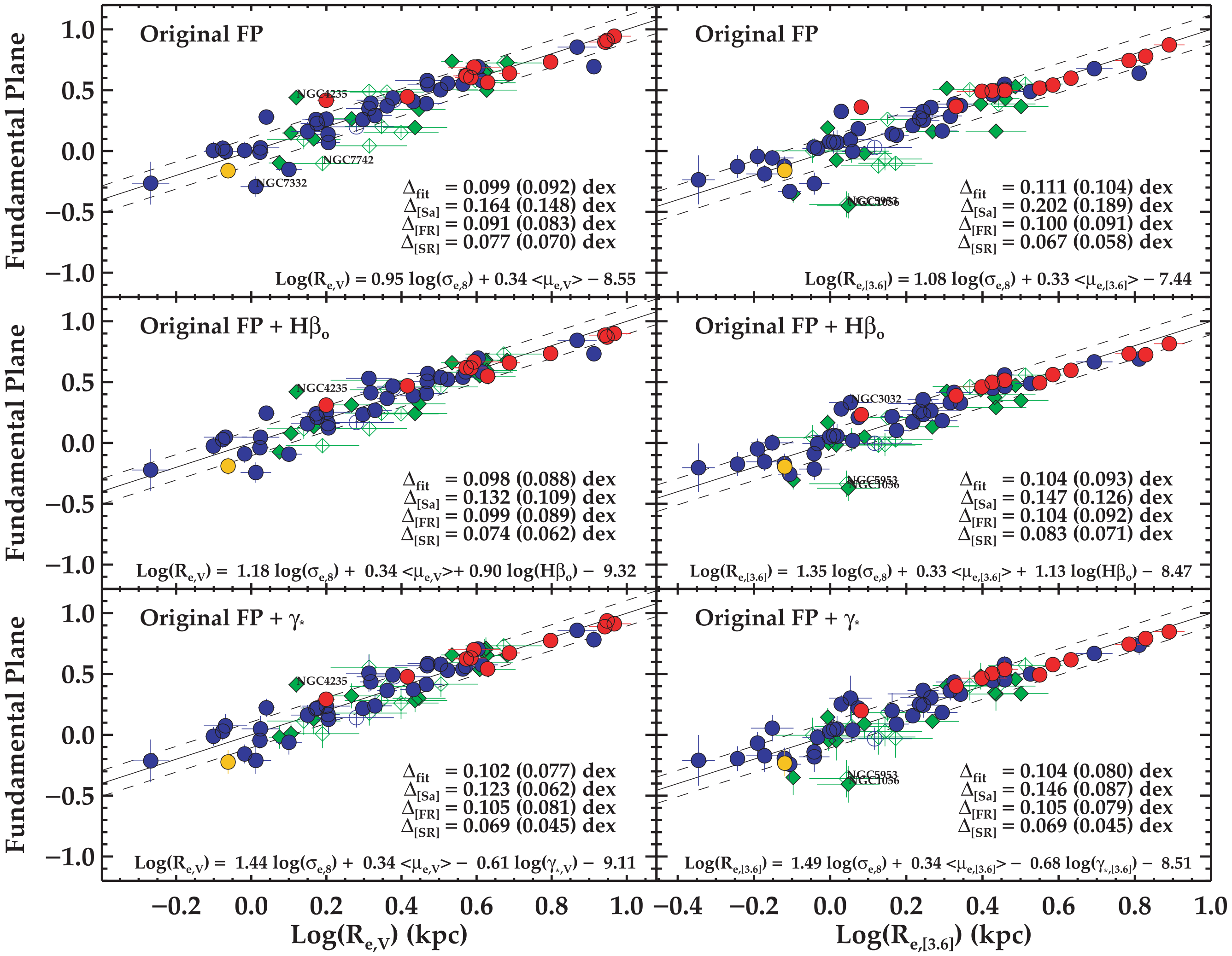

Figure 15. Edge-on views of the FP relations for the galaxies in the SAURON sample in the V and 3.6-μm bands. Here $\sigma_e/8$ ($\sigma_{e,8}$) is used instead of σ_e. Symbols are as in Fig. 3. Top row: original FP relation. Middle row: original FP relation with an Hβ_0 term. Bottom row: original FP relation with a γ_* term. The dashed lines mark the 1σ uncertainty [measured in $\log(R_e)$] considering all objects. The solid line is the best-fitting relation (as indicated in the equation in each panel). $\Delta_{\rm fit}$ indicates the observed and intrinsic scatters (the latter in parentheses) measured along the $\log(R_e)$ axis for the galaxies used to obtain the fit, while $\Delta_{[\ldots]}$ represent the measured values for the different families around the best-fitting relations.

dispersion in a small or large aperture. Alternatively, this result could be due to the shallower nature of the stellar velocity dispersion profiles of the Sa galaxies compared to those of the SR/FR galaxies.

8 CONCLUSIONS

In this paper, we report results from photometric follow-up conducted in the context of the SAURON project. We use ground-based MDM V-band and *Spitzer*/IRAC 3.6-μm-band imaging to characterize our sample of E, S0 and Sa galaxies. We perform aperture photometry to derive homogeneous half-light radii, mean effective surface brightnesses and total magnitudes. Combined with the SAURON integral-field spectroscopic observations, this allows us to explore and understand the location of the galaxies in the main scaling relations as a function of the level of rotation, kinematic substructure, stellar populations and environment.

A number of conclusions can be derived from the work presented and are summarized in the following points:

(i) The level of kinematic substructure (as determined from our stellar kinematic maps) or the environment does not lead to a preferred location in any of the scaling relations investigated. However, this is subject to the potential biases introduced by our sample selection. Our *cluster* environment is defined by the Virgo Cluster and Leo group.

(ii) The SR galaxies define tighter relations than FR galaxies. While this is not totally unexpected (i.e. SRs are uniformly old systems), it is remarkable how the trend is kept both for small and large R_e. We find that the SR and FR galaxies do not populate distinct locations in the scaling relations. The Sa family is the main contributor to the scatters.

(iii) Sa galaxies deviate from the CMR and colour–σ_e relation due to the presence of dust. SR/FR galaxies instead define very tight relations.

(iv) Surprisingly, extremely young objects do not display the bluest (V − [3.6]) colours of our sample, as is usually the case for optical colours. This can be understood in the context of the large contribution of TP-AGB stars to the infrared even for young populations, which makes the $(V - [3.6])$ colour almost insensitive to age for populations above ≈1 Gyr. This effect results in a very tight $(V - [3.6])$–σ_e relation that allows us to define a strong correlation between metallicity and σ_e.

(v) A large number of Sa galaxies appear to follow the main relations defined by earlier-type systems, and are not necessarily offset as previously found. We believe this is due to the use of σ_e (the stellar velocity dispersion integrated within R_e), which is not as much influenced by the presence of young inner discs and accounts to a large extent for rotation in the galaxies.

(vi) FR and Sa galaxies that appear offset from the relations correspond mostly to objects with extremely young populations and signs of ongoing, extended star formation (as already highlighted in Papers XIII and XV). For the specific case of the FP, we made an attempt to correct for this effect so that all galaxies are part of a tight, single relation. Once this is done, the FP coefficients in the V and 3.6-μm bands are the same within the uncertainties. The new estimated coefficients suggest that differences in stellar populations account for about 50 per cent of the observed tilt with respect to the virial prediction.

(vii) The observed scatter of the SR family around the FP is smaller than that of the FR or Sa galaxies. After correcting for stellar populations, the SR family shows almost no intrinsic scatter around the best-fitting FP.

(viii) The use of a velocity dispersion within a small aperture (e.g. $R_e/8$) in the FP results in an increase of around 15 per cent in the intrinsic scatter and an average 10 per cent decrease in the tilt away from the virial relation (as a result of the correlation between R_e and σ_e, given by the SLR and FJR).

We have deliberately focused on the role of stellar populations on the main scaling relations of early-type galaxies. The effects other galaxy properties exert on them (e.g. non-homology, anisotropy and dark matter variations) will be studied in ongoing and upcoming integral-field spectroscopic surveys.

ACKNOWLEDGMENTS

The authors want to thank Maaike Damen, Kambiz Fathi, Katia Ganda, Bettina Gerken and Peter Kamphuis for their contribution to this work and assistance during the observing campaigns at the MDM Observatory. We also thank the referee for very useful comments that have helped improving the presentation of our results. JF-B would like to thank A. Vazdekis and J. A. L. Aguerri for insightful discussions on stellar population models and scaling relations. JF-B and KLS acknowledge the repeated hospitality of the Institute for Advanced Study, to which collaborative visits contributed greatly to the quality of this work. We are grateful to the Isaac Newton Group and MDM staff for their excellent support and assistance during and after the observations. JF-B acknowledges the support from the Ramón y Cajal Program as well as grant AYA2010-21322-C03-02 by the Spanish Ministry of Science and Innovation. HJ acknowledges the support from the International Research Internship Program of the Korea Science and Engineering Foundation. MB and RLD are grateful for the post-doctoral support through STFC rolling grant PP/E001114/1. MC acknowledges the support from a STFC Advanced Fellowship PP/D005574/1 and a Royal Society University Research Fellowship. RMMcD is supported by the Gemini Observatory, which is operated by the Association of Universities for Research in Astronomy, Inc., on behalf of the international Gemini partnership of Argentina, Australia, Brazil, Canada, Chile, the United Kingdom and the United States of America. KLS acknowledge the support from Spitzer Research Award 1359449. SY acknowledges the support from the National Research Foundation of Korea to the Center for Galaxy Evolution Research through Doyak grant (No. 20090078756). The SAURON project is made possible through grants from the NWO and financial contributions from the Institut National des Sciences de l'Univers, the Université Lyon I, the Universities of Durham, Leiden and Oxford, the Programme National Galaxies, the British Council, STFC grant 'Observational Astrophysics at Oxford' and support from Christ Church Oxford and the Netherlands Research School for Astronomy (NOVA). We acknowledge the usage in PPXF of the MPFIT routine by Markwardt (2009). The SAURON observations were obtained at the William Herschel Telescope, operated by the Isaac Newton Group in the Spanish Observatorio del Roque de los Muchachos of the Instituto de Astrofísica de Canarias. This work is based in part on observations made with the *Spitzer Space Telescope*, which is operated by the Jet Propulsion Laboratory, California Institute of Technology under a contract with NASA. This research has made use of the NED which is operated by the Jet Propulsion Laboratory, California Institute of Technology, under contract with the National Aeronautics and Space Administration. We acknowledge the usage of the HyperLeda data base (http://leda.univ-lyon1.fr).

REFERENCES

Allanson S. P., Hudson M. J., Smith R. J., Lucey J. R., 2009, ApJ, 702, 1275

Andreon S., 2006, MNRAS, 369, 969

Arnouts S. et al., 2007, A&A, 476, 137

Bacon R. et al., 2001, MNRAS, 326, 23 (Paper I)

Balcells M., Graham A. W., Peletier R. F., 2007, ApJ, 665, 1104

Baldry I. K., Glazebrook K., Brinkmann J., Ivezić Ž., Lupton R. H., Nichol R. C., Szalay A. S., 2004, ApJ, 600, 681

Bell E. F., de Jong R. S., 2001, ApJ, 550, 212

Bell E. F. et al., 2004, ApJ, 608, 752

Bender R., Burstein D., Faber S. M., 1992, ApJ, 399, 462

Bernardi M. et al., 2003a, AJ, 125, 1817 (B03)

Bernardi M. et al., 2003b, AJ, 125, 1866

Bernardi M., Sheth R. K., Nichol R. C., Schneider D. P., Brinkmann J., 2005, AJ, 129, 61

Bertin E., Arnouts S., 1996, A&AS, 117, 393

Bolton A. S., Treu T., Koopmans L. V. E., Gavazzi R., Moustakas L. A., Burles S., Schlegel D. J., Wayth R., 2008, ApJ, 684, 248

Bower R. G., Lucey J. R., Ellis R. S., 1992, MNRAS, 254, 601

Burstein D., Davies R. L., Dressler A., Faber S. M., Stone R. P. S., Lynden Bell D., Terlevich R. J., Wegner G., 1987, ApJS, 64, 601

Busarello G., Capaccioli M., Capozziello S., Longo G., Puddu E., 1997, A&A, 320, 415

Byun Y. I. et al., 1996, AJ, 111, 1889

Cantiello M., Blakeslee J., Raimondo G., Brocato E., Capaccioli M., 2007, ApJ, 668, 130

Caon N., Capaccioli M., D'Onofrio M., 1993, MNRAS, 265, 1013

Cappellari M., 2002, MNRAS, 333, 400

Cappellari M., Emsellem E., 2004, PASP, 116, 138

Cappellari M. et al., 2006, MNRAS, 366, 1126 (Paper IV)

Cappellari M. et al., 2007, MNRAS, 379, 418 (Paper X)

Cappellari M. et al., 2011, MNRAS, 413, 813

Carlberg R. G., 1984, ApJ, 286, 403

Carollo C. M., Franx M., Illingworth G. D., Forbes D. A., 1997, ApJ, 481, 710

Cervantes J. L., Vazdekis A., 2009, MNRAS, 392, 691

Ciotti L., Bertin G., 1999, A&A, 352, 447

Ciotti L., Lanzoni B., Renzini A., 1996, MNRAS, 282, 1

Combes F., Young L. M., Bureau M., 2007, MNRAS, 377, 1795

Conselice C. J., Bundy K., Ellis R. S., Brichmann J., Vogt N. P., Phillips A. C., 2005, ApJ, 628, 160

Courteau S., Dutton A. A., van den Bosch F. C., MacArthur L. A., Dekel A., McIntosh D. H., Dale D. A., 2007, ApJ, 671, 203

Crook A. C., Huchra J. P., Martimbeau N., Masters K. L., Jarrett T., Macri L. M., 2007, ApJ, 655, 790

D'Onofrio M., Valentinuzzi T., Secco L., Caimmi R., Bindoni D., 2006, New Astron. Rev., 50, 447

de Jong R. S., 2008, MNRAS, 388, 1521

De Lucia G. et al., 2004, ApJ, 610, L77

de Vaucouleurs G., 1961, ApJS, 5, 233

de Vaucouleurs G., de Vaucouleurs A., Corwin J. H. G., Buta R. J., Paturel G., Fouque P., 1991, Third Reference Catalogue of Bright Galaxies. Springer-Verlag, Berlin, Heidelberg, New York

de Zeeuw P. T. et al., 2002, MNRAS, 329, 513 (Paper II)

Djorgovski S., Davis M., 1987, ApJ, 313, 59

Dressler A., Lynden Bell D., Burstein D., Davies R. L., Faber S. M., Terlevich R., Wegner G., 1987, ApJ, 313, 42

Emsellem E. et al., 2004, MNRAS, 352, 721 (Paper III)

Emsellem E. et al., 2007, MNRAS, 379, 401 (Paper IX)

Emsellem E. et al., 2011, MNRAS, 414, 888

Faber S. M., Jackson R. E., 1976, ApJ, 204, 668

Falcón-Barroso J., Peletier R. F., Balcells M., 2002, MNRAS, 335, 741

Falcón-Barroso J., Balcells M., Peletier R. F., Vazdekis A., 2003, A&A, 405, 455

Falcón-Barroso J. et al., 2004, MNRAS, 350, 35

Falcón-Barroso J. et al., 2006, MNRAS, 369, 529 (Paper VII)

Ferrarese L., van den Bosch F. C., Ford H. C., Jaffe W., O'Connell R. W., 1994, AJ, 108, 1598

Freedman W. L. et al., 2001, ApJ, 553, 47

Gallazzi A., Bell E. F., 2009, ApJS, 185, 253

Gargiulo A. et al., 2009, MNRAS, 397, 75

Gebhardt K. et al., 1996, AJ, 112, 105

Girardi L., Bertelli G., 1998, MNRAS, 300, 533

Girardi L., Bressan A., Bertelli G., Chiosi C., 2000, A&AS, 141, 371

Graham A., Colless M., 1997, MNRAS, 287, 221

Graham A., Lauer T. R., Colless M., Postman M., 1996, ApJ, 465, 534

Graves G. J., Faber S. M., 2010, ApJ, 717, 803

Graves G. J., Faber S. M., Schiavon R. P., 2009, ApJ, 693, 486

Guzman R., Lucey J. R., Bower R. G., 1993, MNRAS, 265, 731

Holden B. P. et al., 2005, ApJ, 620, L83

Hyde J. B., Bernardi M., 2009, MNRAS, 396, 1171

Jarrett T. H., Chester T., Cutri R., Schneider S., Skrutskie M., Huchra J. P., 2000, AJ, 119, 2498

Jeong H. et al., 2009, MNRAS, 398, 2028 (Paper XIII)

Jørgensen I., 1999, MNRAS, 306, 607

Jørgensen I., Franx M., Kjaergaard P., 1992, A&AS, 95, 489

Jørgensen I., Franx M., Kjaergaard P., 1995, MNRAS, 273, 1097

Jørgensen I., Franx M., Kjaergaard P., 1996, MNRAS, 280, 167

Kauffmann G. et al., 2003, MNRAS, 341, 33

Kelson D. D., Illingworth G. D., van Dokkum P. G., Franx M., 2000, ApJ, 531, 184

Khosroshahi H. G., Wadadekar Y., Kembhavi A., Mobasher B., 2000, ApJ, 531, L103

Kormendy J., 1977, ApJ, 218, 333

Kormendy J., Fisher D. B., Cornell M. E., Bender R., 2009, ApJS, 182, 216

Krajnović D. et al., 2008, MNRAS, 390, 93 (Paper XII)

Kroupa P., 2001, MNRAS, 322, 231

Kuntschner H., 2000, MNRAS, 315, 184

Kuntschner H. et al., 2006, MNRAS, 369, 497 (Paper VI)

Kuntschner H. et al., 2010, MNRAS, 408, 97 (Paper XVII)

La Barbera F., Busarello G., Capaccioli M., 2000, A&A, 362, 851

La Barbera F., Merluzzi P., Busarello G., Massarotti M., Mercurio A., 2004, A&A, 425, 797

La Barbera F., Busarello G., Merluzzi P., de la Rosa I. G., Coppola G., Haines C. P., 2008, ApJ, 689, 913

La Barbera F., de Carvalho R. R., de La Rosa I. G., Lopes P. A. A., Kohl-Moreira J. L., Capelato H. V., 2010, MNRAS, 408, 1313

Landolt A. U., 1992, AJ, 104, 340

Landsman W. B., 1993, in Hanisch R. J., Brissenden R. J. V., Barnes J., eds, ASP Conf. Ser. Vol. 52, Astronomical Data Analysis Software and Systems II. Astron. Soc. Pac., San Francisco, p. 246

Lauer T. R. et al., 2005, AJ, 129, 2138

Laurikainen E., Salo H., Buta R., Knapen J. H., Comerón S., 2010, MNRAS, 405, 1089

Longhetti M., Saracco P., 2009, MNRAS, 394, 774

MacArthur L. A., 2005, ApJ, 623, 795

MacArthur L. A., Courteau S., Holtzman J. A., 2003, ApJ, 582, 689

MacArthur L. A., Ellis R. S., Treu T., Moran S., 2010, ApJ, 709, 53

McDermid R. M. et al., 2006, MNRAS, 373, 906 (Paper VIII)

Maraston C., 2005, MNRAS, 362, 799

Marigo P., Girardi L., Bressan A., Groenewegen M. A. T., Silva L., Granato G. L., 2008, A&A, 482, 883 (MAR08)

Markwardt C. B., 2009, in Bohlender D. A., Durand D., Dowler P., eds, ASP Conf. Ser. Vol. 411, Non-linear Least-squares Fitting in IDL with MPFIT. Astron. Soc. Pac., San Francisco, p. 251

Mei S. et al., 2007, ApJ, 655, 144

Michard R., 2002, A&A, 384, 763

Mobasher B., Guzman R., Aragon-Salamanca A., Zepf S., 1999, MNRAS, 304, 225

Mould J. R. et al., 2000, ApJ, 529, 786

Nigoche-Netro A., Ruelas-Mayorga A., Franco-Balderas A., 2008, A&A, 491, 731

Nigoche-Netro A., Ruelas-Mayorga A., Franco-Balderas A., 2009, MNRAS, 392, 1060

Pahre M. A., 1999, ApJS, 124, 127

Pahre M. A., Djorgovski S. G., de Carvalho R. R., 1998, AJ, 116, 1591

Panter B., Jimenez R., Heavens A. F., Charlot S., 2007, MNRAS, 378, 1550

Paturel G., 1984, ApJ, 282, 382

Paturel G. et al., 1997, A&AS, 124, 109

Peletier R. F., Davies R. L., Illingworth G. D., Davis L. E., Cawson M., 1990, AJ, 100, 1091

Peletier R. F. et al., 2007, MNRAS, 379, 445 (Paper XI)

Plana H., Boulesteix J., 1996, A&A, 307, 391

Press W. H., Teukolsky S. A., Vetterling W. T., Flannery B. P., 1992, Numerical Recipes in FORTRAN. The Art of Scientific Computing, 2nd edn. Cambridge Univ. Press, Cambridge

Proctor R. N., Lah P., Forbes D. A., Colless M., Couch W., 2008, MNRAS, 386, 1781

Prugniel P., Simien F., 1994, A&A, 282, L1

Prugniel P., Simien F., 1996, A&A, 309, 749

Prugniel P., Simien F., 1997, A&A, 321, 111

Reindl B., Tammann G. A., Sandage A., Saha A., 2005, ApJ, 624, 532

Rest A., van den Bosch F. C., Jaffe W., Tran H., Tsvetanov Z., Ford H. C., Davies J., Schafer J., 2001, AJ, 121, 2431

Rix H., Franx M., Fisher D., Illingworth G., 1992, ApJ, 400, L5

Saglia R. P., Bender R., Dressler A., 1993, A&A, 279, 75

Saglia R. P., Colless M., Burstein D., Davies R. L., McMahan R. K., Wegner G., 2001, MNRAS, 324, 389

Saglia R. P. et al., 2010, A&A, 524, A6

Sánchez-Blázquez P., Gorgas J., Cardiel N., González J. J., 2006a, A&A, 457, 809

Sánchez-Blázquez P. et al., 2006b, MNRAS, 371, 703

Sandage A., 1972, ApJ, 176, 21

Schiavon R. P., 2007, ApJS, 171, 146

Schlegel D. J., Finkbeiner D. P., Davis M., 1998, ApJ, 500, 525

Scott N. et al., 2009, MNRAS, 398, 1835 (Paper XIV)

Sérsic J. L., 1968, Atlas de Galaxias Australes. Observatorio Astronomico, Cordoba, Argentina

Shapiro K. L. et al., 2010, MNRAS, 402, 2140 (Paper XV)

Spergel D. N. et al., 2007, ApJS, 170, 377
Terry J. N., Paturel G., Ekholm T., 2002, A&A, 393, 57
Thomas D., Maraston C., Bender R., Mendes de Oliveira C., 2005, ApJ, 621, 673
Tonry J. L., Dressler A., Blakeslee J. P., Ajhar E. A., Fletcher A. B., Luppino G. A., Metzger M. R., Moore C. B., 2001, ApJ, 546, 681
Trager S. C., Faber S. M., Worthey G., González J. J., 2000, AJ, 120, 165
Tremaine S. et al., 2002, ApJ, 574, 740
Treu T., Koopmans L. V., Bolton A. S., Burles S., Moustakas L. A., 2006, ApJ, 640, 662
Trujillo I., Burkert A., Bell E. F., 2004, ApJ, 600, L39
Trujillo I. et al., 2006, ApJ, 650, 18
Tully R. B., Fisher J. R., 1977, A&A, 54, 661
Tully R. B., Shaya E. J., Karachentsev I. D., Courtois H. M., Kocevski D. D., Rizzi L., Peel A., 2008, ApJ, 676, 184
Valdes F. G., Campusano L. E., Velasquez J. D., Stetson P. B., 1995, PASP, 107, 1119
van der Wel A., Franx M., van Dokkum P. G., Rix H., 2004, ApJ, 601, L5
van Dokkum P. G. et al., 2008, ApJ, 677, L5
Vazdekis A., Sánchez-Blázquez P., Falcón-Barroso J., Cenarro A. J., Beasley M. A., Cardiel N., Gorgas J., Peletier R. F., 2010, MNRAS, 404, 1639 (VAZ10)
Visvanathan N., Sandage A., 1977, ApJ, 216, 214
White S. D. M., 1980, MNRAS, 191, 1p
Willick J. A., Courteau S., Faber S. M., Burstein D., Dekel A., Strauss M. A., 1997, ApJS, 109, 333
Worthey G., 1994, ApJS, 95, 107
Wu H., Shao Z., Mo H. J., Xia X., Deng Z., 2005, ApJ, 622, 244
Zibetti S., Gavazzi G., Scodeggio M., Franzetti P., Boselli A., 2002, ApJ, 579, 261
Zibetti S., Charlot S., Rix H., 2009, MNRAS, 400, 1181
Ziegler B. L., Thomas D., Böhm A., Bender R., Fritz A., Maraston C., 2005, A&A, 433, 519

APPENDIX A: STELLAR POPULATION MODELS

As described in Section 6.1, we use a combination of the new MILES models (VAZ10) together with those of MAR08 to interpret our results. The choice of these models is deliberate. The MILES models currently provide one of the best libraries for the study of stellar populations at optical wavelengths. They are based on the MILES stellar library (Sánchez-Blázquez et al. 2006b) which consists of ≈1000 stars spanning a large range in atmospheric parameters and covering the wavelength range 3525–7500 Å at 2.3 Å (FWHM) spectral resolution. The spectral resolution, spectral type coverage, flux calibration accuracy and number of stars represent a substantial improvement over previous libraries used in population synthesis models. The MAR08 models, on the other hand, provide colour predictions at infrared wavelengths, and in particular for the *Spitzer*/IRAC 3.6-μm band data used here. These models differ from the MILES models in that they have incorporated an improved treatment of the TP-AGB phase. The main advantage is that both libraries make use of the same set of theoretical isochrones (Girardi et al. 2000) and therefore allow us to generate photometric and spectroscopic predictions on the same age and metallicity scales, as well as for the same type of IMF. For the purpose of our work, we focus on predictions for a Kroupa IMF (not corrected for binaries). The spectroscopic measurements have been performed after transforming the MILES models to the LIS-14.0 Å system (see VAZ10).

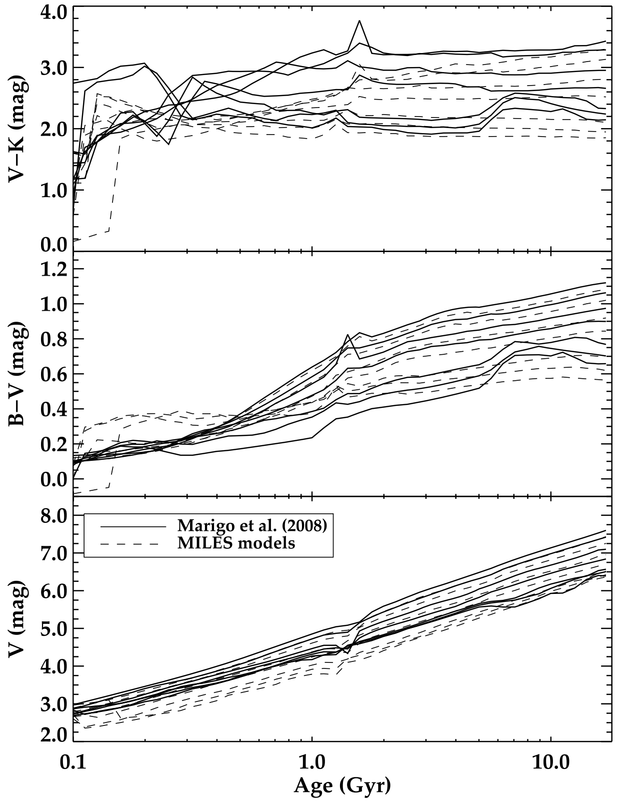

Figure A1. Comparison of the colour and luminosity predictions of the Marigo et al. (2008) and MILES VAZ10 models as a function of age (in Gyr) and metallicity (increasing from −2.32 to +0.22, from bottom to top, with increasing colour or luminosity), for a Kroupa IMF.

Although still somewhat controversial in the details, the importance of the TP-AGB phase on observed colours has been recognized (e.g. Maraston 2005). In order to understand the impact the TP-AGB phase has on the optical and infrared colours used here, we show in Fig. A1 the photometric predictions of both sets of models up to the reddest band predicted by the MILES models (K band). Given the small difference observed between the K and 3.6-μm colours, any conclusion based on the K band can be extended to the *Spitzer*/IRAC 3.6-μm data. The top row shows the $V - K$ colour as a function of age for a range of metallicities. The difference between the MILES and MAR08 models, at large metallicities in particular, is significant. While the MILES models predict a strong correlation between colour and age, this is essentially non-existent for ages above 1 Gyr in the MAR08 models (which show a constant behaviour). This result contrasts with the good agreement, albeit with a small offset, between the two sets of models for the $B - V$ colour (as shown in the middle panel) over the range of ages and metallicities displayed by our data. This is confirmed in the bottom panel, showing that the predicted V-band magnitudes in both sets of models are consistent except for an offset.

The large similarities between the MILES and MAR08 models at optical wavelengths allow us to safely combine the spectroscopic prediction from the MILES and the photometric ones from MAR08 (as shown in Fig. 7).

As shown in Section 6.1, our sample galaxies display a very tight correlation between the $(V - [3.6])_{\mathrm{e}}$ colour and σ_{e}. Transforming that relation into a mass–metallicity relation requires to derive a relation between the $(V - [3.6])_{\mathrm{e}}$ colour and metallicity ([M/H])

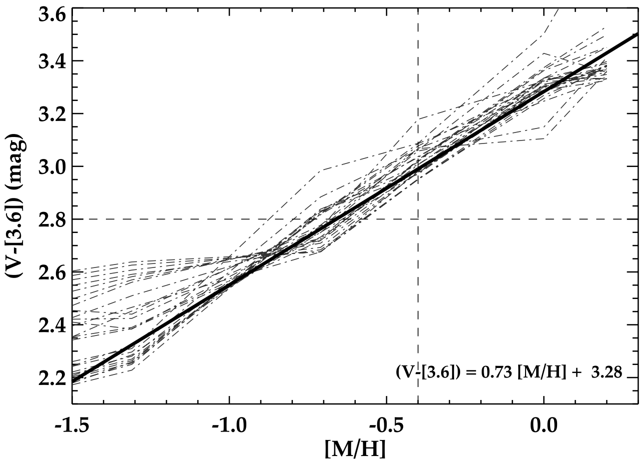

Figure A2. (V − [3.6]) versus metallicity relation from the SSP models of Marigo et al. (2008). The dashed lines mark the predictions for different ages and metallicities. The thick solid line shows the best fit for the range of colours and Hβ_0 values defined by our sample (top right-hand quadrant delimited by the horizontal and vertical dashed lines). The fitted relation is also indicated.

first. This is shown in Fig. A2, based on the MAR08 models for the range of colours and Hβ_0 values exhibited by our sample [$(V - [3.6])_{\rm e} \geq 2.8$ mag and H$\beta_0 \leq 3.0$ Å].

APPENDIX B: STELLAR MASS-TO-LIGHT RATIOS

The effective stellar mass-to-light ratio (γ_*) is one of the most-sought-after quantities when it comes to determine the stellar mass content or to derive the fraction of dark matter present in a galaxy (e.g. after comparison with dynamical estimates). Pioneering work relied on optical and infrared colours (e.g. Bell & de Jong 2001). This has been extended over the years to provide new calibrations based on different sets of filters (Longhetti & Saracco 2009; Zibetti, Charlot & Rix 2009). The use of full spectral fitting methods has also been extensive (e.g. Panter et al. 2007), but as a drawback, it requires some prescription for the amount of dust present in the fitted galaxies. An alternative not much explored is the use of line-strength indices (but see Allanson et al. 2009; Graves & Faber 2010). The advantage is that line-strengths are largely insensitive to the presence of dust (MacArthur 2005) and only a small number of indices are required to get accurate γ_* estimates (Gallazzi & Bell 2009).

Ideally, one would like to use γ_* from models which include a proper treatment of the TP-AGB phase. The MAR08 models, however, do not provide such a quantity. It is possible though to estimate γ_* based on the MILES predictions corrected for the colour differences between the two model libraries (given their consistency in the optical range). For the V band, for instance, we scale the MILES γ_* for the small difference between the models' V-band predictions (bottom panel in Fig. A1). Once this is done, it is possible to determine γ_* at 3.6 µm using the MAR08 $(V - [3.6])_{\rm e}$ colour.

Detailed studies on the SFHs of early-type galaxies show a wide range of scenarios. It does seem, however, that the SFH of a galaxy is largely dependent on its stellar mass (Thomas et al. 2005), with massive galaxies showing SSPs while lower mass galaxies display more extended star formation. The sample considered here consists of early-type galaxies as well as Sa disc galaxies. A priori the expected range of SFHs is quite large, given the range of SSP quantities exhibited (see Papers XI and XVII). While full, non-parametric spectral fitting is desirable in principle, it is not clear whether and how the short SAURON spectral range will provide more constraints than those from the Hβ, Hβ_0, Fe5015 and Mg*b* line-strength indices (i.e. the main features in our wavelength range).

We choose here to use as baseline SFHs different combinations of two stellar populations. While a library with different combinations might not accurately represent the SFH of any given galaxy, it will at least show the maximum range of γ_* allowed for a given pair of Hβ_0 and [MgFe50]′ indices. We thus built a library of $\sim 5 \times 10^6$ models by combining two SSPs in the age range from 0.1 to 17.28 Gyr (sampled logarithmically) and [M/H] = [−2.32, 0.22] (sampled uniformly) for different mass fractions of the young component

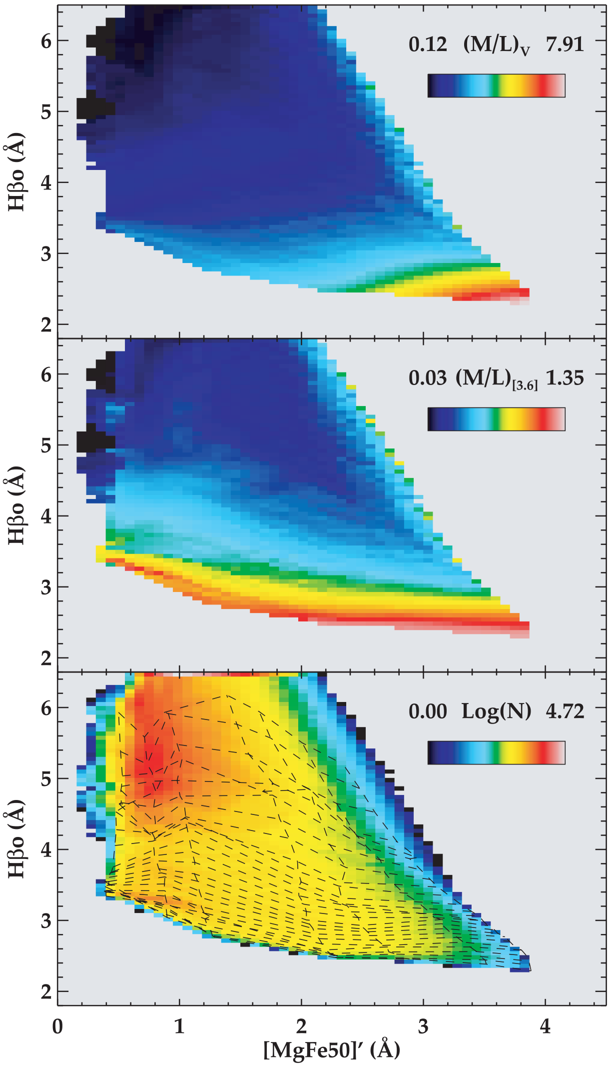

Figure B1. Stellar mass-to-light ratio (γ_*) predictions for the set of models produced by the combination of two SSPs. The top and middle panels show the median M/L in the V and 3.6-µm bands. The bottom panel shows a two-dimensional diagram with the number of models (in logarithmic scale) falling in a given bin in the Hβ_0 versus [MgFe50]′ space. For reference, the dashed lines mark locations of equal age (along the vertical direction) and metallicity (along the abcissae) for a SSP.

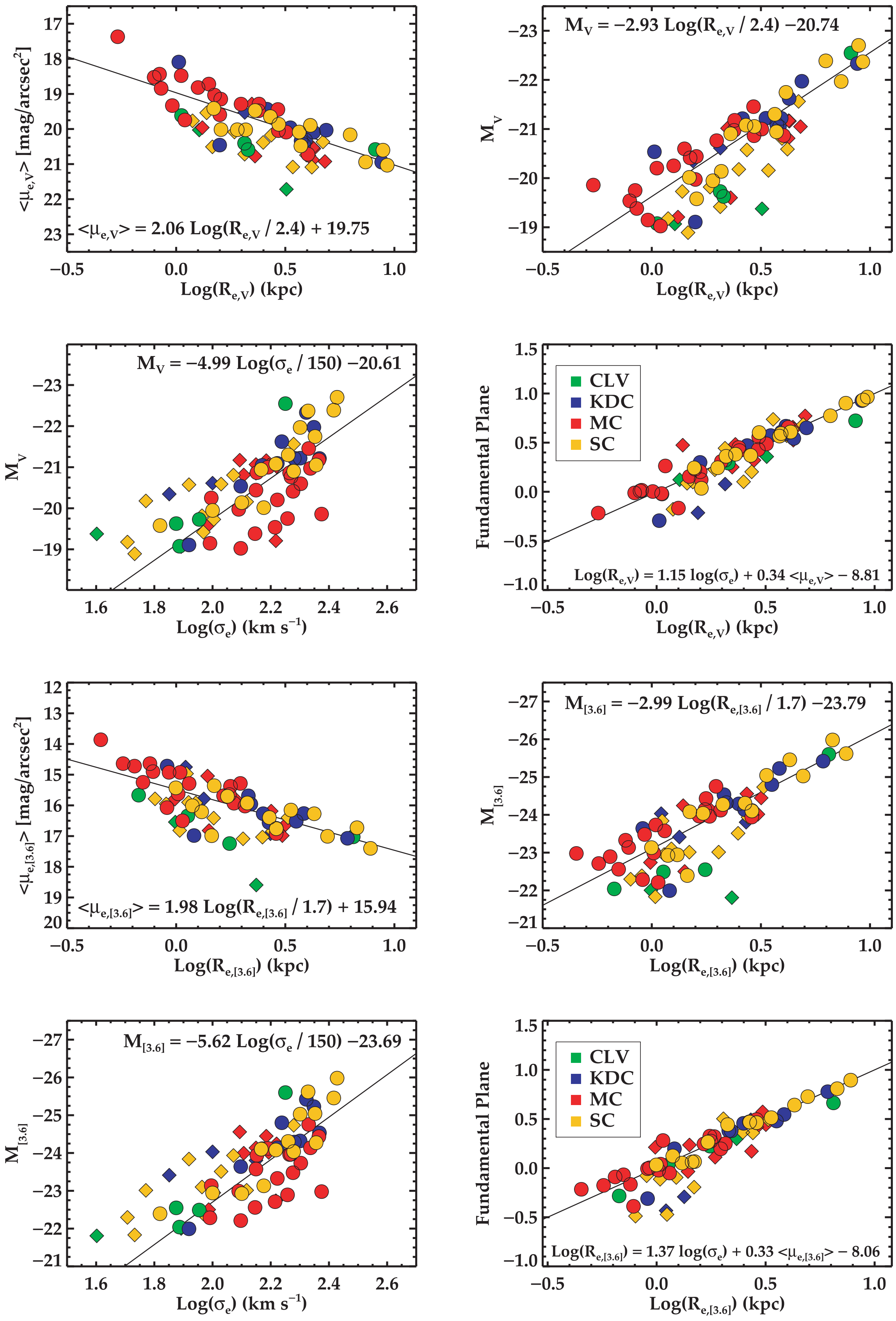

Figure C1. Scaling relations in the *V* and 3.6-μm bands for the SAURON sample. Galaxies are colour-coded according to their level of kinematic substructure: (CLV) central low velocity, (KDC) kinematically decoupled core, (MC) multiple component and (SC) single component. Elliptical and lenticular galaxies are marked with the circles, while Sa galaxies are denoted with the diamonds. Best-fitting relations are as shown in Sections 6 and 7.

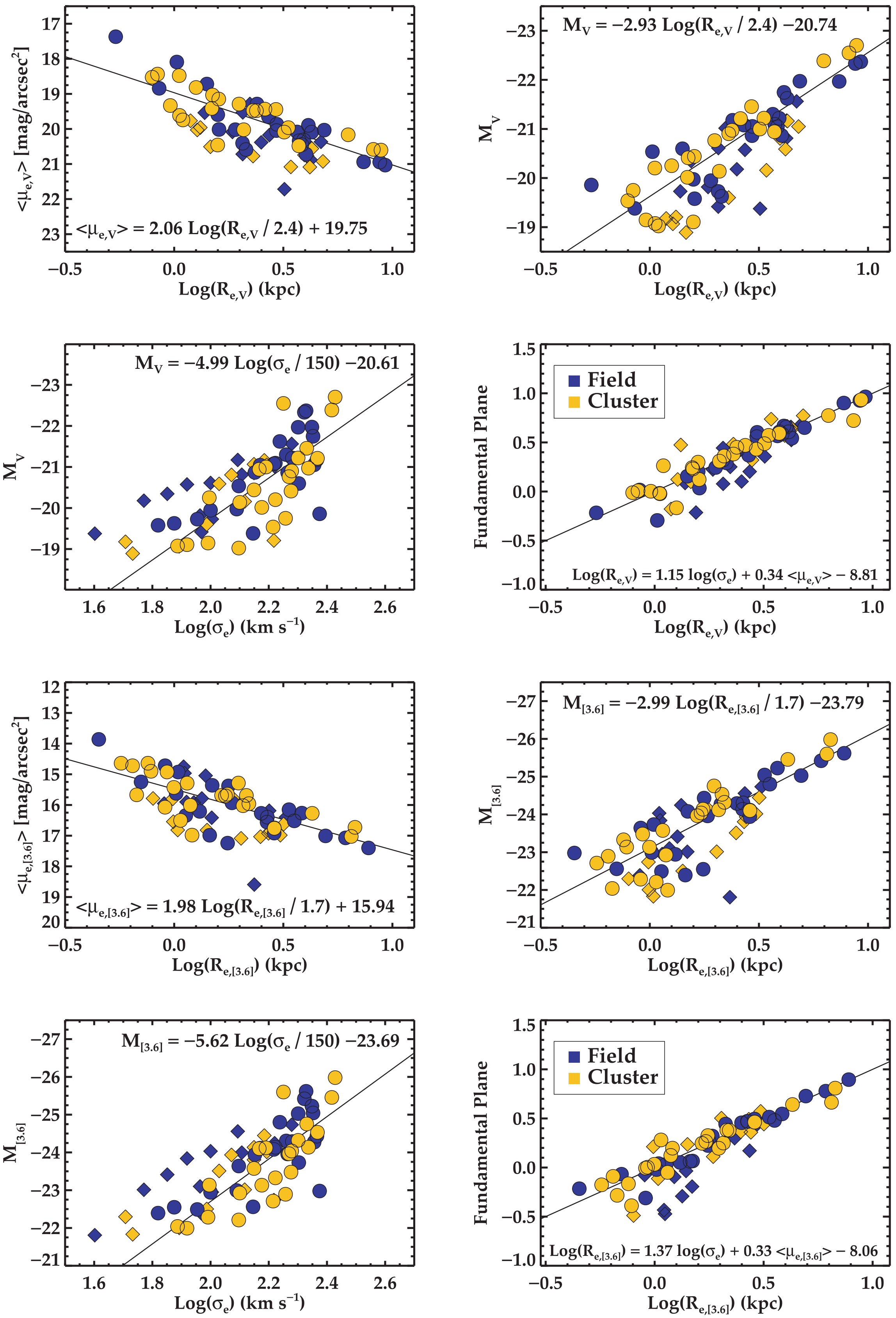

Figure C2. Scaling relations in the *V* and 3.6-μm bands for the SAURON sample. Galaxies are colour-coded according to their environment as indicated. Elliptical and lenticular galaxies are marked with the circles, while Sa galaxies are denoted with the diamonds. Best-fitting relations are as shown in Sections 6 and 7.

from 0 (i.e. an SSP) to 0.25. We set no restriction on the metallicities of the two components and simply impose the age of the young one to be lower than the old one. Fig. B1 shows the median γ_*, for the V and 3.6-μm bands, in the Hβ_0 versus [MgFe50]′ space. It also shows the number of models per bin. On average our library of models contain at least 1000 predictions per bin. Fig. B1 shows that γ_* variations depend mostly on Hβ_0 and that this dependency is stronger in the 3.6-μm band than in the V band.

We determine the best effective γ_* via a Bayesian approach following Kauffmann et al. (2003) (see appendix A in that paper

Table D1. Photometric quantities for the SAURON sample of E/S0 galaxies.

Galaxy (1)	Environment (2)	D (Mpc) (3)	Reference (4)	$R_{\mathrm{e},V}$ (arcsec) (5)	$\langle\mu_{\mathrm{e},V}\rangle$ (mag arcsec^{-2}) (6)	M_V (mag) (7)	A$_V$ (mag) (8)	$R_{\mathrm{e},[3.6]}$ (arcsec) (9)	$\langle\mu_{\mathrm{e},[3.6]}\rangle$ (mag arcsec^{-2}) (10)	$M_{[3.6]}$ (mag) (11)	$A_{[3.6]}$ (mag) (12)	$(V-[3.6])_\mathrm{e}$ (mag) (13)	n_V (14)	$n_{[3.6]}$ (15)
0474	F	29.51	1	28.08 ± 1.65	20.72 ± 0.09	−20.87 ± 0.12	0.11	20.07 ± 0.37	20.72 ± 0.11	−23.94 ± 0.11	0.01	3.26 ± 0.05	4.0	4.0
0524	F	23.99	3	35.41 ± 1.02	19.90 ± 0.07	−21.75 ± 0.20	0.27	28.86 ± 0.26	19.90 ± 0.08	−25.04 ± 0.20	0.02	3.43 ± 0.03	2.8	2.8
0821	F	24.10	3	31.33 ± 1.49	20.09 ± 0.08	−21.30 ± 0.17	0.36	22.88 ± 0.46	20.09 ± 0.10	−24.31 ± 0.17	0.02	3.19 ± 0.04	4.0	4.0
1023	F	11.43	3	48.75 ± 1.46	19.65 ± 0.05	−21.08 ± 0.16	0.20	26.95 ± 0.19	19.65 ± 0.08	−24.08 ± 0.16	0.01	3.35 ± 0.02	4.0	3.0
2549	F	12.65	3	13.92 ± 0.43	18.84 ± 0.16	−19.38 ± 0.28	0.21	11.49 ± 0.08	18.84 ± 0.19	−22.56 ± 0.28	0.01	3.30 ± 0.02	2.9	2.9
2685	F	16.60	0	23.68 ± 1.16	20.02 ± 0.10	−19.95 ± 0.49	0.20	16.27 ± 0.41	20.02 ± 0.14	−22.94 ± 0.49	0.01	3.21 ± 0.04	4.0	3.5
2695	F	32.36	3	18.74 ± 1.26	20.05 ± 0.12	−20.86 ± 0.40	0.06	11.72 ± 0.13	20.05 ± 0.19	−23.96 ± 0.40	0.00	3.37 ± 0.04	4.0	3.1
2699	F	26.92	3	12.14 ± 0.95	19.59 ± 0.18	−19.97 ± 0.27	0.07	7.83 ± 0.08	19.59 ± 0.28	−22.99 ± 0.27	0.00	3.29 ± 0.05	4.0	2.9
2768	F	22.39	3	67.97 ± 3.11	20.94 ± 0.05	−21.97 ± 0.24	0.14	45.49 ± 0.28	20.94 ± 0.05	−25.03 ± 0.24	0.01	3.29 ± 0.04	4.0	3.5
2974	F	21.48	3	28.35 ± 1.61	19.87 ± 0.09	−21.05 ± 0.24	0.18	20.33 ± 0.11	19.87 ± 0.11	−24.27 ± 0.24	0.01	3.42 ± 0.04	4.0	3.4
3032	F	21.98	3	19.30 ± 1.07	20.41 ± 0.12	−19.73 ± 0.28	0.06	10.61 ± 0.09	20.41 ± 0.20	−22.49 ± 0.28	0.00	3.08 ± 0.04	3.6	3.6
3156	F	22.39	3	14.78 ± 0.44	20.02 ± 0.15	−19.58 ± 0.14	0.11	13.40 ± 0.14	20.02 ± 0.16	−22.39 ± 0.14	0.01	2.89 ± 0.03	2.4	2.4
3377	C	11.22	3	38.28 ± 1.99	20.02 ± 0.07	−20.14 ± 0.10	0.11	21.80 ± 0.22	20.02 ± 0.10	−22.92 ± 0.09	0.01	3.08 ± 0.04	4.0	4.0
3379	C	10.57	3	44.89 ± 1.47	19.47 ± 0.05	−20.90 ± 0.11	0.08	33.53 ± 0.40	19.47 ± 0.07	−24.04 ± 0.11	0.00	3.31 ± 0.03	4.0	4.0
3384	C	11.59	3	28.50 ± 0.91	19.15 ± 0.08	−20.44 ± 0.14	0.09	20.41 ± 0.09	19.15 ± 0.11	−23.57 ± 0.14	0.00	3.28 ± 0.02	4.0	4.0
3414	F	25.23	3	32.02 ± 1.45	20.31 ± 0.08	−21.22 ± 0.33	0.08	20.47 ± 0.23	20.31 ± 0.11	−24.29 ± 0.33	0.00	3.31 ± 0.03	4.0	4.0
3489	C	12.08	3	21.51 ± 0.81	18.82 ± 0.10	−20.25 ± 0.15	0.05	13.38 ± 0.14	18.82 ± 0.16	−23.14 ± 0.15	0.00	3.15 ± 0.02	4.0	3.0
3608	F	22.91	3	33.64 ± 1.52	20.34 ± 0.07	−21.09 ± 0.14	0.07	23.98 ± 0.15	20.34 ± 0.09	−24.14 ± 0.14	0.00	3.24 ± 0.04	4.0	4.0
4150	C	13.74	3	15.88 ± 0.52	19.62 ± 0.14	−19.07 ± 0.24	0.06	10.10 ± 0.09	19.62 ± 0.21	−22.04 ± 0.24	0.00	3.24 ± 0.02	2.6	2.6
4262	C	15.42	2	10.60 ± 0.43	18.53 ± 0.21	−19.54 ± 0.06	0.11	7.64 ± 0.07	18.53 ± 0.28	−22.71 ± 0.06	0.01	3.34 ± 0.02	4.0	4.0
4270	C	16.53	5	13.68 ± 0.47	19.74 ± 0.16	−19.02 ± 0.09	0.07	13.34 ± 0.14	19.74 ± 0.16	−22.21 ± 0.08	0.00	3.21 ± 0.03	2.2	2.2
4278	C	16.07	3	30.57 ± 1.07	19.48 ± 0.07	−20.97 ± 0.20	0.09	22.51 ± 0.39	19.48 ± 0.10	−24.14 ± 0.20	0.00	3.32 ± 0.02	4.0	4.0
4374	C	18.45	2	70.08 ± 2.95	20.17 ± 0.04	−22.39 ± 0.06	0.13	47.95 ± 0.60	20.17 ± 0.05	−25.46 ± 0.05	0.01	3.28 ± 0.03	4.0	4.0
4382	C	17.86	2	94.40 ± 3.17	20.58 ± 0.04	−22.55 ± 0.06	0.10	74.77 ± 0.70	20.58 ± 0.03	−25.60 ± 0.05	0.01	3.21 ± 0.04	4.0	4.0
4387	C	17.95	2	11.04 ± 0.22	19.33 ± 0.20	−19.15 ± 0.06	0.11	10.43 ± 0.08	19.33 ± 0.21	−22.28 ± 0.06	0.01	3.18 ± 0.02	2.1	2.1
4458	C	16.37	2	19.94 ± 0.96	20.46 ± 0.12	−19.11 ± 0.06	0.08	15.21 ± 0.14	20.46 ± 0.14	−21.99 ± 0.05	0.00	3.07 ± 0.04	3.1	2.9
4459	C	16.07	2	40.97 ± 1.48	20.09 ± 0.06	−21.00 ± 0.07	0.15	26.54 ± 0.36	20.09 ± 0.08	−24.12 ± 0.06	0.01	3.35 ± 0.03	4.0	4.0
4473	C	15.28	2	26.76 ± 0.89	19.29 ± 0.08	−20.76 ± 0.06	0.09	22.26 ± 0.31	19.29 ± 0.10	−23.97 ± 0.06	0.00	3.30 ± 0.02	4.0	4.4
4477	C	16.53	5	46.48 ± 2.22	20.48 ± 0.06	−20.94 ± 0.09	0.10	35.87 ± 0.69	20.48 ± 0.06	−24.10 ± 0.08	0.01	3.32 ± 0.04	4.0	4.0
4486	C	17.22	2	106.18 ± 4.23	20.60 ± 0.05	−22.70 ± 0.08	0.07	80.69 ± 0.71	20.60 ± 0.03	−25.98 ± 0.07	0.00	3.44 ± 0.04	4.0	4.0
4526	C	16.90	3	35.70 ± 1.29	19.44 ± 0.07	−21.46 ± 0.20	0.07	24.03 ± 0.22	19.44 ± 0.09	−24.75 ± 0.20	0.00	3.53 ± 0.03	3.3	3.2
4546	C	14.06	3	21.98 ± 0.94	19.03 ± 0.10	−20.41 ± 0.20	0.11	13.60 ± 0.10	19.03 ± 0.16	−23.48 ± 0.20	0.01	3.34 ± 0.03	4.0	3.4
4550	C	15.49	2	11.55 ± 0.27	19.00 ± 0.19	−19.26 ± 0.05	0.13	10.13 ± 0.06	19.00 ± 0.21	−22.30 ± 0.05	0.01	3.15 ± 0.02	1.8	1.8
4552	C	15.85	2	33.89 ± 1.09	19.43 ± 0.07	−21.21 ± 0.06	0.13	27.88 ± 0.21	19.43 ± 0.08	−24.53 ± 0.06	0.01	3.43 ± 0.02	4.0	4.0
4564	C	15.85	2	19.35 ± 1.11	19.41 ± 0.12	−20.02 ± 0.07	0.11	12.97 ± 0.21	19.41 ± 0.17	−23.13 ± 0.06	0.01	3.34 ± 0.04	4.0	3.4
4570	C	17.06	2	12.75 ± 0.56	18.48 ± 0.17	−20.20 ± 0.07	0.07	9.17 ± 0.08	18.48 ± 0.24	−23.33 ± 0.06	0.00	3.34 ± 0.03	4.0	2.4
4621	C	14.93	2	46.06 ± 2.99	19.96 ± 0.06	−21.22 ± 0.07	0.11	30.38 ± 0.39	19.96 ± 0.07	−24.32 ± 0.06	0.01	3.33 ± 0.04	4.0	4.0
4660	C	15.00	2	11.54 ± 0.41	18.44 ± 0.19	−19.75 ± 0.05	0.11	8.87 ± 0.11	18.44 ± 0.25	−22.89 ± 0.05	0.01	3.31 ± 0.02	4.0	4.0
5198	F	48.78	8	18.01 ± 0.69	20.09 ± 0.12	−21.62 ± 0.03	0.08	15.01 ± 0.14	20.09 ± 0.14	−24.80 ± 0.01	0.00	3.31 ± 0.03	2.5	2.5
5308	F	29.43	4	9.89 ± 0.25	18.72 ± 0.22	−20.60 ± 0.22	0.06	7.31 ± 0.04	18.72 ± 0.30	−23.73 ± 0.22	0.00	3.38 ± 0.02	4.0	1.7
5813	F	32.21	3	55.99 ± 2.72	20.94 ± 0.06	−22.33 ± 0.19	0.19	39.03 ± 0.62	20.94 ± 0.06	−25.42 ± 0.18	0.01	3.33 ± 0.05	4.0	4.0
5831	F	27.16	3	29.19 ± 1.70	20.45 ± 0.08	−21.04 ± 0.17	0.19	21.82 ± 0.27	20.45 ± 0.10	−24.11 ± 0.17	0.01	3.23 ± 0.04	4.0	4.0
5838	F	23.99	0	20.61 ± 0.87	19.29 ± 0.11	−21.18 ± 0.49	0.17	15.25 ± 0.12	19.29 ± 0.14	−24.43 ± 0.49	0.01	3.41 ± 0.03	4.0	3.8
5845	F	25.94	3	4.29 ± 0.26	17.37 ± 0.51	−19.86 ± 0.21	0.17	3.59 ± 0.08	17.37 ± 0.61	−22.98 ± 0.21	0.01	3.29 ± 0.05	4.0	4.0
5846	F	24.89	3	76.79 ± 3.32	21.03 ± 0.05	−22.37 ± 0.21	0.18	64.39 ± 0.61	21.03 ± 0.04	−25.62 ± 0.20	0.01	3.35 ± 0.05	4.0	4.0
5982	F	40.36	1	24.89 ± 1.19	20.03 ± 0.09	−21.97 ± 0.09	0.06	19.65 ± 0.19	20.03 ± 0.11	−25.23 ± 0.09	0.00	3.38 ± 0.03	4.0	4.0
7332	F	23.01	3	9.21 ± 0.15	18.09 ± 0.24	−20.54 ± 0.20	0.12	8.14 ± 0.04	18.09 ± 0.27	−23.64 ± 0.20	0.01	3.20 ± 0.01	2.0	2.0
7457	F	13.24	3	33.25 ± 1.28	20.59 ± 0.08	−19.63 ± 0.21	0.17	27.37 ± 0.19	20.59 ± 0.08	−22.55 ± 0.21	0.01	3.08 ± 0.04	2.5	2.5

Notes. Column (1): NGC galaxy number. Column (2): environment: field (F) or cluster (C). Column (3): distance (Mpc). Column (4): original reference for the distance estimate [0: redshift distance from the NED; 1: Cantiello et al. (2007); 2: Mei et al. (2007); 3: Tonry et al. (2001); 4: Reindl et al. (2005); 5: Mei et al. (2007), but see method (iii) in Section 3.3; 6: Terry et al. (2002); 7: Tully et al. (2008); 8: Willick et al. (1997)]. See Section 3.3 for uncertainties in the measurements. Columns (5–12): photometric quantities – effective radii (R_e), mean effective surface brightness ($\langle\mu_\mathrm{e}\rangle$), absolute magnitude ($M$) and Galactic extinction in the V and 3.6-μm bands. Column (13): effective ($V-[3.6]$) colour. Columns (14) and (15): Sérsic indices used in our growth curve analysis (see Section 4).

Table D2. Photometric quantities for the SAURON sample of Sa galaxies.

Galaxy (1)	Environment (2)	D (Mpc) (3)	Reference (4)	$R_{\mathrm{e},V}$ (arcsec) (5)	$\langle\mu_{\mathrm{e},V}\rangle$ (mag arcsec^{-2}) (6)	M_V (mag) (7)	A_V (mag) (8)	$R_{\mathrm{e},[3.6]}$ (arcsec) (9)	$\langle\mu_{\mathrm{e},[3.6]}\rangle$ (mag arcsec^{-2}) (10)	$M_{[3.6]}$ (mag) (11)	$A_{[3.6]}$ (mag) (12)	$(V-[3.6])_\mathrm{e}$ (mag) (13)	n_V (14)	$n_{[3.6]}$ (15)
1056	F	32.21	7	17.48 ± 1.24	20.17 ± 0.13	−20.57 ± 0.40	0.48	7.14 ± 0.32	20.17 ± 0.31	−23.84 ± 0.40	0.03	3.70 ± 0.06	4.0	4.0
2273	F	31.62	6	27.64 ± 1.22	20.53 ± 0.09	−21.17 ± 0.39	0.23	17.78 ± 0.65	20.53 ± 0.12	−24.56 ± 0.39	0.01	3.64 ± 0.04	2.9	6.6
2844	F	25.12	0	16.91 ± 1.23	20.72 ± 0.14	−19.42 ± 0.49	0.06	7.39 ± 0.11	20.72 ± 0.29	−22.39 ± 0.49	0.00	3.41 ± 0.05	4.0	2.9
3623	C	11.97	7	48.21 ± 0.95	19.73 ± 0.05	−21.07 ± 0.35	0.08	31.99 ± 0.32	19.73 ± 0.07	−24.14 ± 0.35	0.00	3.45 ± 0.03	2.1	1.5
4220	F	18.79	7	20.30 ± 0.50	20.08 ± 0.11	−19.82 ± 0.36	0.06	13.50 ± 0.08	20.08 ± 0.16	−23.10 ± 0.36	0.00	3.62 ± 0.03	1.6	2.1
4235	C	16.53	5	16.44 ± 0.49	19.96 ± 0.13	−19.21 ± 0.09	0.06	12.30 ± 0.24	19.96 ± 0.18	−22.74 ± 0.08	0.00	3.71 ± 0.03	1.9	1.9
4245	C	13.18	0	35.95 ± 1.63	20.77 ± 0.07	−19.60 ± 0.49	0.07	22.14 ± 0.23	20.77 ± 0.10	−22.50 ± 0.49	0.00	3.24 ± 0.04	3.5	3.5
4274	C	19.41	7	45.43 ± 1.26	20.56 ± 0.06	−21.16 ± 0.36	0.07	33.70 ± 0.16	20.56 ± 0.06	−24.45 ± 0.36	0.00	3.53 ± 0.03	2.3	1.6
4293	C	16.53	5	52.20 ± 1.63	21.09 ± 0.06	−20.59 ± 0.09	0.13	31.00 ± 0.48	21.09 ± 0.07	−23.51 ± 0.08	0.01	3.36 ± 0.05	1.8	2.4
4314	C	17.38	0	46.90 ± 2.24	20.74 ± 0.06	−20.81 ± 0.49	0.08	32.80 ± 0.59	20.74 ± 0.07	−23.94 ± 0.49	0.00	3.31 ± 0.03	4.0	3.0
4369	F	20.89	0	24.73 ± 1.27	20.38 ± 0.09	−20.18 ± 0.49	0.08	14.67 ± 0.15	20.38 ± 0.15	−23.01 ± 0.49	0.00	3.13 ± 0.04	4.0	2.7
4383	C	16.53	5	14.83 ± 0.79	19.77 ± 0.15	−19.18 ± 0.09	0.08	9.98 ± 0.19	19.77 ± 0.22	−22.30 ± 0.08	0.00	3.32 ± 0.03	4.0	4.0
4405	C	16.53	5	18.29 ± 0.48	20.51 ± 0.12	−18.89 ± 0.09	0.08	12.95 ± 0.17	20.51 ± 0.17	−21.83 ± 0.08	0.00	3.25 ± 0.04	1.2	1.2
4425	C	16.53	5	15.91 ± 0.65	20.03 ± 0.14	−19.07 ± 0.09	0.09	12.36 ± 0.09	20.03 ± 0.18	−22.00 ± 0.08	0.00	3.14 ± 0.04	2.0	2.0
4596	C	16.53	5	59.91 ± 3.05	20.93 ± 0.06	−21.05 ± 0.09	0.07	38.24 ± 0.45	20.93 ± 0.06	−24.02 ± 0.08	0.00	3.25 ± 0.05	4.0	4.0
4698	C	16.53	5	50.64 ± 2.40	20.76 ± 0.06	−20.85 ± 0.09	0.08	33.74 ± 0.22	20.76 ± 0.06	−23.80 ± 0.08	0.00	3.22 ± 0.04	4.0	3.0
4772	C	16.53	5	42.71 ± 2.34	21.08 ± 0.07	−20.16 ± 0.09	0.09	25.26 ± 0.31	21.08 ± 0.09	−23.01 ± 0.08	0.00	3.14 ± 0.05	4.0	4.0
5448	F	34.83	6	24.97 ± 0.87	20.88 ± 0.10	−20.81 ± 0.18	0.05	17.09 ± 0.26	20.88 ± 0.13	−24.00 ± 0.18	0.00	3.48 ± 0.04	1.8	3.0
5475	F	30.20	0	9.42 ± 0.23	19.54 ± 0.23	−19.73 ± 0.49	0.04	7.78 ± 0.07	19.54 ± 0.28	−22.95 ± 0.49	0.00	3.36 ± 0.02	1.3	2.4
5636	F	28.84	0	22.89 ± 0.89	21.72 ± 0.11	−19.38 ± 0.49	0.11	16.65 ± 0.24	21.72 ± 0.13	−21.81 ± 0.49	0.01	2.85 ± 0.07	1.0	1.0
5689	F	36.31	0	12.63 ± 0.35	19.29 ± 0.17	−21.02 ± 0.49	0.12	7.91 ± 0.04	19.29 ± 0.27	−24.24 ± 0.49	0.01	3.56 ± 0.03	2.1	2.1
5953	F	33.11	0	12.84 ± 0.72	19.53 ± 0.17	−20.61 ± 0.49	0.16	6.88 ± 0.14	19.53 ± 0.32	−24.03 ± 0.49	0.01	3.71 ± 0.04	4.0	4.0
6501	F	47.86	0	20.27 ± 1.40	20.37 ± 0.12	−21.56 ± 0.49	0.29	14.02 ± 0.33	20.37 ± 0.16	−24.73 ± 0.49	0.02	3.35 ± 0.05	4.0	5.9
7742	F	22.91	0	13.93 ± 0.36	19.17 ± 0.16	−20.35 ± 0.49	0.18	12.05 ± 0.07	19.17 ± 0.18	−23.41 ± 0.49	0.01	3.18 ± 0.02	2.1	2.1

Notes. Column (1): NGC galaxy number. Column (2): environment: field (F) or cluster (C). Column (3): distance (Mpc). Column (4): original reference for the distance estimate [0: redshift distance from the NED; 1: Cantiello et al. (2007); 2: Mei et al. (2007); 3: Tonry et al. (2001); 4: Reindl et al. (2005); 5: Mei et al. (2007), but see (iii) in Section 3.3; 6: Terry et al. (2002); 7: Tully et al. (2008); 8: Willick et al. (1997)]. See Section 3.3 for uncertainties in the measurements. Columns (5–12): photometric quantities – effective radii (R_e), mean effective surface brightness ($\langle\mu_\mathrm{e}\rangle$), absolute magnitude ($M$) and Galactic extinction in the V and 3.6-μm bands. Column (13): effective ($V-[3.6]$) colour. Columns (14) and (15): Sérsic indices used in our growth curve analysis (see Section 4).

for details). This method results into a probability distribution for a given set of plausible models. We take as effective γ_* the weighted mean value of the distribution and the 68 per cent confidence interval as its uncertainty. Measured values are listed in Tables D3 and D4.

APPENDIX C: DEPENDENCE OF KINEMATIC SUBSTRUCTURE AND ENVIRONMENT IN SCALING RELATIONS

In this appendix, we show the main scaling relations in the V and 3.6-μm bands, colour-coded according to kinematic substructure and environment. They are shown here, rather than in the main text, for completeness as they do not reveal any particular trend.

APPENDIX D: PHOTOMETRIC AND SAURON QUANTITIES

Here we present tables with the aperture photometry derived for the SAURON sample galaxies in both the V and 3.6-μm bands, as described in the text (see Section 4). We also give tables with the spectroscopic quantities derived from the SAURON data, as described in Section 5 and Appendix B.

Table D3. Spectroscopic quantities for the SAURON sample of E/S0 galaxies.

Galaxy (1)	SR/FR (2)	Kinematic substructure (3)	$\sigma_{\rm e}$ (km s^{-1}) (4)	Hβ (Å) (5)	Hβ_0 (Å) (6)	Fe5015 (Å) (7)	Mgb (Å) (8)	$\Upsilon_{*,V}$ $(M_\odot/L_\odot)_V$ (9)	$\Upsilon_{*,[3.6]}$ $(M_\odot/L_\odot)_{[3.6]}$ (10)
0474	FR	MC	142	1.85	2.93	3.84	2.96	$3.52^{+0.67}_{-0.59}$	$0.78^{+0.14}_{-0.13}$
0524	FR	SC	225	1.52	2.58	4.26	3.63	$5.36^{+0.58}_{-0.60}$	$1.05^{+0.10}_{-0.10}$
0821	FR	SC	182	1.65	2.65	3.69	3.22	$4.54^{+0.63}_{-0.60}$	$1.02^{+0.12}_{-0.12}$
1023	FR	SC	165	1.57	2.55	3.85	3.55	$5.17^{+0.56}_{-0.57}$	$1.09^{+0.11}_{-0.11}$
2549	FR	MC	140	2.01	3.26	4.14	3.10	$2.68^{+0.90}_{-0.65}$	$0.53^{+0.17}_{-0.13}$
2685	FR	SC	100	2.05	3.09	3.33	2.59	$2.88^{+0.74}_{-0.69}$	$0.72^{+0.18}_{-0.18}$
2695	FR	MC	184	1.36	2.19	3.39	3.44	$5.01^{+0.28}_{-0.28}$	$1.21^{+0.03}_{-0.05}$
2699	FR	MC	123	1.78	2.83	3.81	3.11	$3.91^{+0.65}_{-0.57}$	$0.87^{+0.13}_{-0.13}$
2768	FR	SC	200	1.67	2.67	3.47	3.12	$4.28^{+0.65}_{-0.62}$	$1.02^{+0.12}_{-0.13}$
2974	FR	SC	227	1.73	2.77	4.01	3.50	$4.33^{+0.60}_{-0.56}$	$0.89^{+0.11}_{-0.12}$
3032	FR	CLV	90	3.85	5.30	3.19	1.74	$1.31^{+0.85}_{-0.58}$	$0.30^{+0.20}_{-0.14}$
3156	FR	SC	66	2.93	4.16	2.90	1.55	$1.45^{+0.70}_{-0.47}$	$0.41^{+0.22}_{-0.14}$
3377	FR	SC	126	1.95	3.10	3.48	2.74	$2.88^{+0.72}_{-0.68}$	$0.69^{+0.17}_{-0.17}$
3379	FR	SC	190	1.54	2.60	3.74	3.53	$4.90^{+0.58}_{-0.59}$	$1.06^{+0.11}_{-0.11}$
3384	FR	MC	141	1.87	2.98	4.05	3.17	$3.40^{+0.66}_{-0.64}$	$0.71^{+0.13}_{-0.14}$
3414	SR	KDC	191	1.58	2.47	3.49	3.17	$4.74^{+0.45}_{-0.43}$	$1.14^{+0.08}_{-0.09}$
3489	FR	MC	99	2.53	3.65	3.47	2.21	$1.94^{+0.78}_{-0.54}$	$0.46^{+0.20}_{-0.15}$
3608	SR	KDC	167	1.71	2.78	3.73	3.24	$4.10^{+0.64}_{-0.59}$	$0.91^{+0.12}_{-0.13}$
4150	FR	CLV	77	2.69	3.57	3.27	2.00	$2.02^{+0.79}_{-0.60}$	$0.52^{+0.22}_{-0.17}$
4262	FR	MC	164	1.52	2.45	3.45	3.33	$4.84^{+0.42}_{-0.43}$	$1.15^{+0.07}_{-0.09}$
4270	FR	MC	125	1.77	2.72	3.64	2.77	$4.10^{+0.68}_{-0.63}$	$0.98^{+0.13}_{-0.13}$
4278	FR	MC	217	1.65	2.73	3.62	3.63	$4.37^{+0.63}_{-0.57}$	$0.95^{+0.12}_{-0.12}$
4374	SR	SC	261	1.49	2.48	3.61	3.47	$5.06^{+0.48}_{-0.48}$	$1.14^{+0.08}_{-0.10}$
4382	FR	CLV	178	1.99	3.09	3.63	2.80	$2.93^{+0.71}_{-0.66}$	$0.67^{+0.16}_{-0.16}$
4387	FR	MC	98	1.60	2.51	3.58	3.18	$4.78^{+0.49}_{-0.49}$	$1.12^{+0.09}_{-0.11}$
4458	SR	KDC	83	1.64	2.46	3.17	2.88	$4.18^{+0.36}_{-0.37}$	$1.15^{+0.08}_{-0.10}$
4459	FR	MC	155	1.92	3.07	3.62	2.91	$2.99^{+0.70}_{-0.68}$	$0.68^{+0.16}_{-0.16}$
4473	FR	MC	186	1.56	2.54	3.82	3.45	$5.11^{+0.54}_{-0.57}$	$1.10^{+0.10}_{-0.11}$
4477	FR	SC	147	1.60	2.61	3.70	3.29	$4.71^{+0.59}_{-0.59}$	$1.05^{+0.12}_{-0.12}$
4486	SR	SC	268	1.25	2.21	3.52	3.87	$5.56^{+0.30}_{-0.30}$	$1.21^{+0.03}_{-0.05}$
4526	FR	MC	214	1.68	2.70	3.89	3.58	$4.61^{+0.61}_{-0.56}$	$0.96^{+0.11}_{-0.11}$
4546	FR	MC	189	1.60	2.49	3.64	3.39	$5.02^{+0.48}_{-0.49}$	$1.13^{+0.09}_{-0.10}$
4550	SR	SC	103	2.01	3.06	3.46	2.55	$2.97^{+0.73}_{-0.69}$	$0.73^{+0.17}_{-0.17}$
4552	SR	KDC	233	1.55	2.64	4.06	3.79	$5.03^{+0.60}_{-0.58}$	$1.00^{+0.10}_{-0.10}$
4564	FR	SC	150	1.62	2.65	3.84	3.47	$4.75^{+0.62}_{-0.59}$	$1.01^{+0.11}_{-0.11}$
4570	FR	MC	167	1.51	2.45	3.75	3.43	$5.24^{+0.45}_{-0.47}$	$1.15^{+0.08}_{-0.09}$
4621	FR	KDC	200	1.50	2.41	3.70	3.56	$5.34^{+0.41}_{-0.44}$	$1.17^{+0.06}_{-0.09}$
4660	FR	MC	181	1.55	2.59	3.72	3.48	$4.89^{+0.59}_{-0.57}$	$1.07^{+0.11}_{-0.11}$
5198	SR	KDC	173	1.60	2.59	3.75	3.43	$4.89^{+0.58}_{-0.57}$	$1.07^{+0.11}_{-0.11}$
5308	FR	MC	201	1.52	2.49	3.83	3.60	$5.36^{+0.50}_{-0.53}$	$1.13^{+0.09}_{-0.10}$
5813	SR	KDC	210	1.54	2.61	3.75	3.47	$4.84^{+0.59}_{-0.59}$	$1.05^{+0.12}_{-0.11}$
5831	SR	KDC	148	1.87	2.96	3.86	2.87	$3.40^{+0.68}_{-0.62}$	$0.76^{+0.15}_{-0.14}$
5838	FR	MC	232	1.66	2.67	3.94	3.58	$4.76^{+0.62}_{-0.57}$	$0.99^{+0.11}_{-0.11}$
5845	FR	MC	237	1.57	2.65	4.19	3.76	$5.03^{+0.61}_{-0.57}$	$0.99^{+0.10}_{-0.10}$
5846	SR	SC	213	1.35	2.36	3.74	3.60	$5.48^{+0.37}_{-0.42}$	$1.18^{+0.05}_{-0.09}$
5982	SR	KDC	223	1.63	2.66	4.05	3.38	$4.79^{+0.62}_{-0.57}$	$1.00^{+0.11}_{-0.11}$
7332	FR	KDC	125	2.10	3.27	3.87	2.75	$2.53^{+0.76}_{-0.61}$	$0.55^{+0.17}_{-0.14}$
7457	FR	CLV	75	2.26	3.40	3.60	2.40	$2.27^{+0.75}_{-0.59}$	$0.53^{+0.19}_{-0.15}$

Notes: Column (1): NGC galaxy number. Column (2): SR/FR class. Column (3): kinematic substructure as defined in Paper XII. Column (4): stellar velocity dispersion within $R_{{\rm e},V}$. Columns (5–8): line-strength indices within $R_{{\rm e},V}$ measured in the LIS-14 Å system. Columns (9) and (10): stellar mass-to-light ratios (Υ_*) in the V and 3.6-μm bands.

Table D4. Spectroscopic quantities for the SAURON sample of Sa galaxies.

Galaxy (1)	SR/FR (2)	Kinematic substructure (3)	$\sigma_{\rm e}$ (km s^{-1}) (4)	Hβ (Å) (5)	Hβ_0 (Å) (6)	Fe5015 (Å) (7)	Mgb (Å) (8)	$\Upsilon_{*,V}$ $(M_\odot/L_\odot)_V$ (9)	$\Upsilon_{*,[3.6]}$ $(M_\odot/L_\odot)_{[3.6]}$ (10)
1056	FR	SC	83	2.85	3.94	1.76	1.24	$1.47^{+0.46}_{-0.41}$	$0.60^{+0.18}_{-0.14}$
2273	FR	MC	124	2.72	3.98	3.13	2.27	$1.63^{+0.75}_{-0.50}$	$0.40^{+0.20}_{-0.14}$
2844	FR	SC	93	2.45	3.49	2.56	1.70	$1.96^{+0.75}_{-0.61}$	$0.64^{+0.23}_{-0.21}$
3623	FR	MC	141	1.69	2.70	3.70	3.27	$4.39^{+0.65}_{-0.59}$	$0.98^{+0.12}_{-0.12}$
4220	FR	SC	92	2.61	3.68	3.89	2.40	$2.04^{+0.83}_{-0.59}$	$0.43^{+0.17}_{-0.13}$
4235	FR	MC	165	1.84	2.69	3.67	2.97	$4.29^{+0.66}_{-0.61}$	$1.00^{+0.13}_{-0.13}$
4245	FR	MC	97	1.94	2.95	3.43	2.76	$3.31^{+0.73}_{-0.63}$	$0.81^{+0.16}_{-0.14}$
4274	FR	MC	153	1.88	2.89	3.51	2.85	$3.53^{+0.71}_{-0.62}$	$0.85^{+0.15}_{-0.14}$
4293	FR	SC	107	2.44	3.53	3.71	2.30	$2.12^{+0.79}_{-0.56}$	$0.48^{+0.20}_{-0.14}$
4314	FR	SC	118	2.13	3.13	3.37	2.60	$2.79^{+0.74}_{-0.70}$	$0.69^{+0.18}_{-0.18}$
4369	FR	SC	59	3.39	4.72	1.99	1.30	$1.07^{+0.60}_{-0.41}$	$0.36^{+0.21}_{-0.15}$
4383	FR	SC	51	3.05	4.05	0.40	0.89	$1.15^{+0.40}_{-0.25}$	$0.63^{+0.25}_{-0.10}$
4405	FR	SC	54	3.13	4.36	2.34	1.53	$1.21^{+0.64}_{-0.37}$	$0.37^{+0.24}_{-0.12}$
4425	FR	CLV	78	1.89	2.90	3.62	2.78	$3.52^{+0.70}_{-0.62}$	$0.83^{+0.15}_{-0.14}$
4596	FR	MC	156	1.66	2.62	3.51	3.21	$4.49^{+0.61}_{-0.58}$	$1.05^{+0.12}_{-0.12}$
4698	FR	KDC	141	1.67	2.59	3.30	2.90	$4.20^{+0.53}_{-0.55}$	$1.08^{+0.11}_{-0.13}$
4772	FR	SC	131	1.54	2.50	3.07	3.19	$4.27^{+0.42}_{-0.43}$	$1.13^{+0.09}_{-0.11}$
5448	FR	MC	128	2.19	3.27	3.23	2.65	$2.50^{+0.79}_{-0.68}$	$0.62^{+0.20}_{-0.18}$
5475	FR	SC	101	2.17	3.35	4.07	2.85	$2.49^{+0.88}_{-0.62}$	$0.51^{+0.17}_{-0.13}$
5636	FR	CLV	40	2.49	3.64	2.53	1.75	$1.81^{+0.73}_{-0.59}$	$0.58^{+0.24}_{-0.20}$
5689	FR	MC	166	1.98	3.12	4.02	2.93	$2.91^{+0.74}_{-0.64}$	$0.61^{+0.15}_{-0.14}$
5953	FR	KDC	100	2.86	3.97	1.69	1.29	$1.44^{+0.46}_{-0.39}$	$0.60^{+0.18}_{-0.14}$
6501	FR	SC	190	1.65	2.65	4.06	3.58	$4.91^{+0.61}_{-0.57}$	$1.00^{+0.11}_{-0.11}$
7742	FR	KDC	71	2.81	4.07	2.87	2.04	$1.53^{+0.72}_{-0.49}$	$0.40^{+0.21}_{-0.14}$

Notes. Column (1): NGC galaxy number. Column (2): SR/FR class. Column (3): kinematic substructure as defined in Paper XII. Column (4): stellar velocity dispersion within $R_{{\rm e},V}$. Columns (5–8): line-strength indices within $R_{{\rm e},V}$ measured in the LIS-14 Å system. Columns (9) and (10): stellar mass-to-light ratios (Υ_*) in the V and 3.6-μm bands.

This paper has been typeset from a TEX/LATEX file prepared by the author.